# ARV

CLIMATE POSITIVE CIRCULAR COMMUNITIES

D7.2 ARCHETYPE BUILDING MODELS

WP7 EFFICIENT OPERATION AND FLEXIBILITY

Tomáš Bäumelt, CVUT
Vladislav Martínek, CVUT
Sofiane Kichou, CVUT
Shahab Tohidi, DTU
Henrik Madsen, DTU
Razgar Ebrahimy, DTU
Alessandra Insana, POLITO
Marco Barla, POLITO
Simone De Feudis, POLITO
Gianluca Grazieschi, EURAC
Ivan Bellanco, IREC
Thibault Péan, IREC
Jaume Salom, IREC
Khadija Barhmi, UU
Andreas Aamodt, SINTEF
Harald Taxt Walnum, SINTEF
Benjamín Manrique Delgado, SINTEF

30. 8. 2024
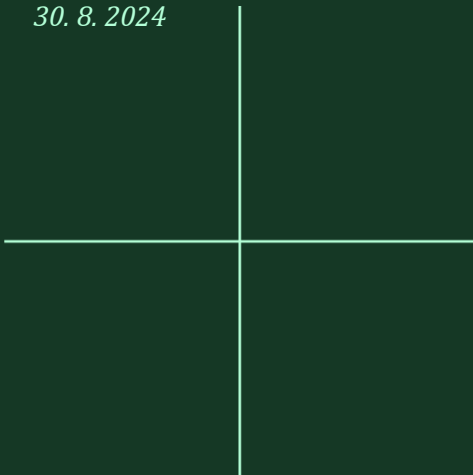
PROJECT INFORMATION

Project acronym	ARV[1]
Project title	Climate Positive Circular Communities
Project number	101036723
Coordinator	Norwegian University of Science and Technology / Inger Andresen
Website	www.GreenDeal-ARV.eu

DOCUMENT INFORMATION

Deliverable Number and Title	D7.2 Archetype building models
Due Month	Month 32 (August 2024)
Work Package Number and Title	WP 7. Efficient Operation and Flexibility
Task number and Title	Task 7.3 Models for energy-efficient operation of buildings and districts
Dissemination Level	PU = Public, fully open
Date of Delivery	30.08.2024
Lead Author	Tomáš Bäumelt, Czech Technical University in Prague (CVUT)
Contributors	Vladislav Martínek (CVUT), Sofiane Kichou (CVUT), Shahab Tohidi (DTU), Henrik Madsen (DTU), Razgar Ebrahimy (DTU), Alessandra Insana (POLITO), Marco Barla

---

	(POLITO), Simone De Feudis (POLITO), Gianluca Grazieschi (EURAC), Ivan Bellanco (IREC), Thibault Péan (IREC), Jaume Salom (IREC), Khadija Barhmi (UU), Andreas Aamodt (SINTEF), Harald Taxt Walnum (SINTEF), Benjamín Manrique Delgado (SINTEF)			
Reviewers	Åse Lekang Sørensen, SINTEF			
Status	Final version V0.3			
Revision Log	Version	Author	Main changes	Date
	V.01	Tomáš Bäumelt, CVUT Vladislav Martínek, CVUT Sofiane Kichou, CVUT Ivan Bellanco, IREC Thibault Péan, IREC Jaume Salom, IREC Harald Taxt Walnum, SINTEF	First draft	11.4.2023
	V.02	Tomáš Bäumelt, CVUT Vladislav Martínek, CVUT Sofiane Kichou, CVUT Shahab Tohidi, DTU Henrik Madsen, DTU Razgar Ebrahimy, DTU Alessandra Insana, POLITO Marco Barla, POLITO Simone De Feudis, POLITO Gianluca Grazieschi, EURAC Ivan Bellanco, IREC Thibault Péan, IREC Jaume Salom, IREC Khadija Barhmi, UU Andreas Aamodt, SINTEF Harald Taxt Walnum, SINTEF Benjamín Manrique Delgado, SINTEF	Second draft	12.8.2024
	V.03	Tomáš Bäumelt, CVUT Vladislav Martínek, CVUT Sofiane Kichou, CVUT Shahab Tohidi, DTU Henrik Madsen, DTU Razgar Ebrahimy, DTU Alessandra Insana, POLITO Marco Barla, POLITO Simone De Feudis, POLITO Gianluca Grazieschi, EURAC Ivan Bellanco, IREC Thibault Péan, IREC Jaume Salom, IREC	Reviewed final draft	29.8.2024

Khadija Barhmi, UU
Andreas Aamodt, SINTEF
Harald Taxt Walnum, SINTEF
Benjamín Manrique Delgado,
SINTEF

ABOUT THE ARV PROJECT

The vision of the ARV project is to contribute to speedy and wide scale implementation of Climate Positive Circular Communities (CPCC) where people can thrive and prosper for generations to come. The overall aim is to demonstrate and validate attractive, resilient, and affordable solutions for CPCC that will significantly speed up the deep energy renovations and the deployment of energy and climate measures in the construction and energy industries. To achieve this, the ARV project will employ a novel concept relying on a combination of 3 conceptual pillars, 6 demonstration projects, and 9 thematic focus areas.

The 3 conceptual pillars are integration, circularity, and simplicity. Integration in ARV means the coupling of people, buildings, and energy systems, through multi-stakeholder co-creation and use of innovative digital tools. Circularity in ARV means a systematic way of addressing circular economy through integrated use of Life Cycle Assessment, digital logbooks, and material banks. Simplicity in ARV means to make the solutions easy to understand and use for all stakeholders, from manufacturers to end-users.

The 6 demonstration projects are urban regeneration projects in 6 locations around Europe. They have been carefully selected to represent the different European climates and contexts, and due to their high ambitions in environmental, social, and economic sustainability. Renovation of social housing and public buildings are specifically focused. Together, they will demonstrate more than 50 innovations in more than 150,000 m² of buildings.

The 9 thematic focus areas are 1) Effective planning and implementation of CPCCs, 2) Enhancing citizen engagement, environment, and well-being, 3) Sustainable building re(design) 4) Resource efficient manufacturing and construction workflows, 5) Smart integration of renewables and storage systems, 6) Effective management of energy and flexibility, 7) Continuous monitoring and evaluation, 8) New business models and financial mechanisms, policy instruments and exploitation, and 9) Effective communication, dissemination, and stakeholder outreach.
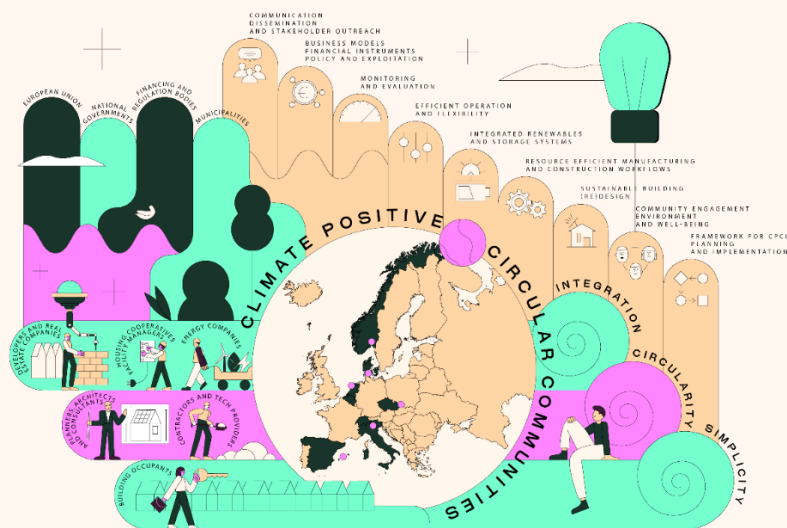
The ARV project is an Innovation Action that has received funding under the Green Deal Call LC-GD-4-1-2020 - Building and renovating in an energy and resource efficient way. The project started in January 2022 and has a project period of 4 years, until December 2025. The project is coordinated by the Norwegian University of Science and Technology and involves 35 partners from 8 different European Countries.

EXECUTIVE SUMMARY

This document is Deliverable D7.2 of Work Package 7 (WP7) in the ARV project. The focus of the report is on the deployment of solutions to optimize the performance of demo sites using advanced building modeling techniques. The primary objective is to identify and describe models that support energy-efficient operations of buildings and districts.

The report is divided into two main parts: an overview of archetype-building modeling methods and demo examples from six case studies across the EU.

Archetype Building Models (ABEMs) are models that represent groups of buildings with similar characteristics. They offer a generalized view of energy consumption patterns across a wide range of buildings. These models are crucial for urban energy planning, policy evaluation, and building stock analysis. They offer the advantage of reduced computational complexity and enhanced scalability, making them ideal for large-scale analyses. The document details two main types of modeling methods for creating ABEMs: physics-based and data-driven approaches. Physics-based models rely on the physical properties of buildings and energy modeling software to predict energy consumption. On the other hand, data-driven models utilize statistical and machine learning methods to analyze real-world data and derive energy consumption patterns.

The report includes six case studies that demonstrate the usage of these models in real-world scenarios:

- Sønderborg, Denmark: The case study focuses on the modeling of a district heating system, demonstrating the potential for energy savings and efficiency improvements.

- Trento, Italy: The study showcases the use of long-term geothermal storage for heat supply, highlighting the potential of such renewable energy sources.

- Palma, Spain: The focus is on centralized HVAC systems in apartment buildings, demonstrating the potential for energy savings through optimized operations.

- Karviná, Czechia & Utrecht, Netherlands: The two case studies focus on PV forecasting and battery storage optimization, showcasing the potential for integrating renewable energy sources and storage solutions in building operations.

- Oslo, Norway: The study demonstrates the use of low-order models for heat pumps and building envelopes, highlighting the potential for energy savings through optimized building design and operations.

The models presented in the report are used for performance assessment and optimization in other parts of the ARV project, such as WP6 and WP7. They provide valuable insights into the potential for energy savings and efficiency improvements in building operations.

TABLE OF CONTENTS

1 INTRODUCTION

Work Package 7 (WP7) focuses on deploying solutions to optimize the performance of demo sites in the ARV project. Since advanced building systems often require modeling to operate efficiently, deliverable D7.2 aims to introduce relevant modeling techniques and showcase examples within ARV demonstration sites. The primary objective of this deliverable is to identify and describe models that support energy-efficient operation of both buildings and districts.

Unlike individually tailored building models, which are usually more accurate but also very labor-intensive, there are archetype building models. These models are general representations of buildings that are very suitable for energy assessment across building stocks, particularly energy efficiency evaluation, energy policy making, and sustainable urban planning.

The report consists of two main parts: a general overview of archetype-building modeling methods and demo examples of using the models. The essential contribution of this deliverable is to present methodologies for building modeling and implementation. The examples in the deliverable D7.2 are given for six different case studies across the EU.

The first demo example in Sønderborg in Denmark deals with a district heating model. The second case study in Trento, Italy, describes the model and presents results for the long-term geothermal storage for the heat supply of the district. The third demo in Spanish Palma presents models for centralized HVAC systems in apartment buildings. Both models for thermal components (a heat pump with storage tanks) and electric components (PV) are presented. Another two case studies deal with PV forecasting, modeling PV, and battery storage. The demos are located in Karviná, Czechia, and Utrecht, the Netherlands. The last section is devoted to the Norwegian case study in Oslo, which presents low-order models (called FLEXor) for heat pumps and building envelopes.

The case studies presented in the report show not only model structures but also calibrated models, identified parameters, and operational data when using them. However, some demo examples in the report (with a deadline in M24) could not demonstrate the full operation of advanced control since ongoing renovation processes have not allowed the usage of proposed models or to show gathered data.

Finally, the given models, findings, and examples from the deliverable D7.2 will be used for the model-based control and generally in performance assessment in other parts of the project, such as WP6 to document demo cases and WP7 for further operation optimization.

2 ARCHETYPAL MODELING OBJECTIVES

The building sector significantly impacts energy consumption and greenhouse gas emissions, accounting for roughly 36 % of global energy use and 40 % of CO_2 emissions [1]. Accurate and reliable building energy models are essential tools for understanding building energy consumption patterns, identifying energy-saving opportunities, and guiding decision-making for energy conservation measures [2]. Archetype building energy models (ABEMs), which represent groups of buildings with similar characteristics, offer a generalized view of energy consumption in the built environment [3]. This report aims to comprehensively analyze the methods and approaches used to construct engineering-based ABEMs and explore their various applications.

The concept of ABEMs arose from the necessity to simplify and generalize the analysis of extensive building stocks [4]. Analyzing each individual building within an examined area, e.g., a city, is computationally demanding when considering numerous variations in building characteristics, usage

patterns, and construction details. ABEMs resolve this challenge by representing buildings with common features like construction type, age, size, and energy consumption characteristics.

The primary goal of ABEMs is to create a simplified yet representative model of building energy consumption. These models are utilized to estimate the overall energy performance of building stocks, identify potential energy-saving measures, and evaluate energy-saving strategies. ABEMs have become crucial urban energy planning, policy evaluation, and building stock analysis tools. They offer several benefits over individual building energy modeling, e.g., reduced computational complexity and enhanced scalability.

Despite being a common tool, a generally accepted or universal standard for ABEMs is yet to be available. It is rather a concept that integrates different approaches (data-driven, physics-based, or hybrid, i.e., a combination of more methods), different levels of building elements and systems that are considered (envelope, zoning, technical systems, e.g., HVAC), and different mathematical models (static, dynamic). A general overview of these techniques will be given in the following section of this document.

3   BUILDING ARCHETYPE MODELLING METHODS

In general, all methods are based on a deep analysis of individual building features, such as envelope properties, building geometry, construction type, HVAC system, and occupancy patterns (Fig. 1). These features and their respective parameters are then calibrated using available data, then an ABEM is created, and its performance can be simulated.
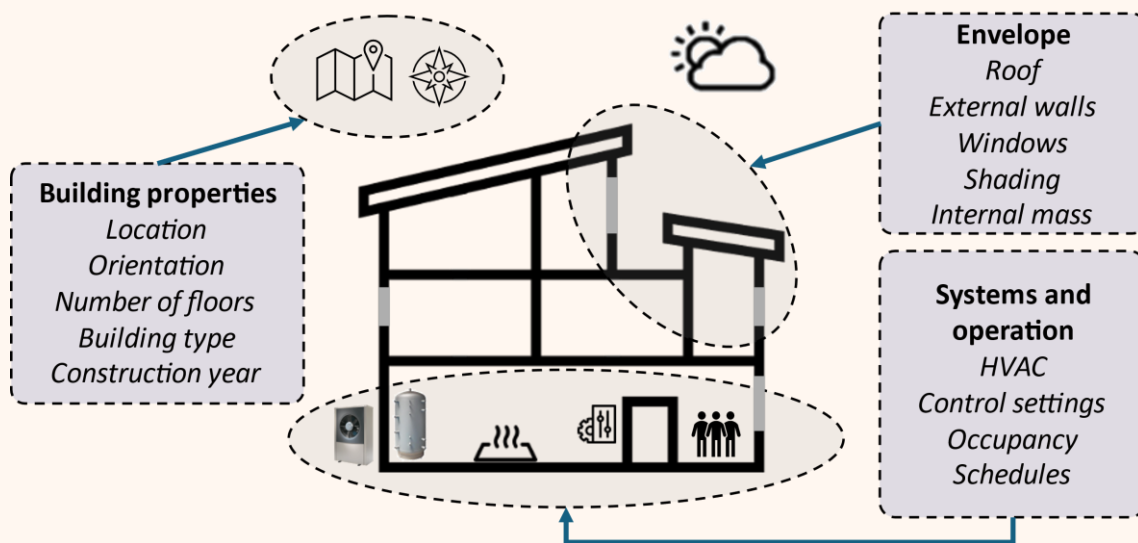

Fig. 1 Building archetype modeling features.

A standard process to obtain and define ABEMs can be described in three main steps before simulation:

1.   Classification of buildings into archetypes,

2.   Characterization of archetype parameters,

3.   Calibration and validation of uncertain archetype parameters.

The building properties are usually used for the first step of the building stocks segmentation (see the left-hand side of Fig. 1. These simple parameters are often available in public databases, such as geographic information systems (GIS) and property registers. The following steps of the procedure are

usually more difficult since there are many issues with data availability, such as legal constraints and privacy considerations. Due to all the different variations amongst the archetype training group and uncertainties in data, it is very unlikely to expect that the ABM should be a purely deterministic model. The model should also incorporate the probabilistic nature of its parameters instead of working only with mean values.

3.1 PHYSICS-BASED MODELS

The first introduced ABEM method is so-called physics-based as its parameters directly represent building physics properties, and it also relies on the building energy modeling software tools. The standard procedure requires several steps.

First, it is necessary to analyze the examined building stock and identify the most suitable candidates representing the most typical buildings in each category. The characteristics of these candidates are then determined from available data sources, e.g., building codes, energy audits, or statistical analysis.

When developing ABMs, it is crucial to consider a range of factors to ensure the models accurately represent the target building typology. These factors encompass building design and configuration, construction materials, energy systems, operational and management practices, and occupant behavior. Essentially, the key factors in ABMs can be categorized into geometric-related and non-geometric parameters.

Geometric-related factors include building design and configuration, such as shape, size, orientation, and layout, significantly influencing energy performance.

Non-geometric factors include the thermal properties of construction materials, such as the building envelope, insulation, and windows, which directly affect heat transfer and heating and cooling loads. The configuration of building energy systems, including HVAC, lighting, and appliances, also plays a significant role in building energy consumption, with variations in efficiency, control strategies, and maintenance leading to differences in energy use. Operational practices like HVAC setpoints, lighting control, and maintenance routines further influence energy performance, and recent studies have focused on modeling these aspects [5].

Occupants' behavior, such as appliance use, window opening, etc., are increasingly recognized as crucial factors affecting building energy use [6]. Incorporating realistic occupant behavior models into ABMs has been shown to significantly enhance their accuracy, with studies indicating that variations in these behaviors can result in up to a 50 % difference in energy use [7]. There is a growing interest in integrating these diverse factors into ABMs to better reflect the complexity of real-world buildings. Various methods, including classic statistical techniques and machine learning, have been employed to characterize these factors for ABMs, which will be discussed in detail in subsequent sections.

The physics-based method can yield detailed and accurate results with hourly resolution, offering a comprehensive understanding of energy performance across various building types [8,9]. However, this approach can be time-consuming and computationally intensive [10] as it involves modeling individual building characteristics and simulating their energy performance using special building energy modeling tools like Energy+ or TRNSYS. These requirements pose challenges when dealing with large building stocks or limited data availability. Despite these difficulties, this method remains crucial for providing reliable and detailed insights into building energy consumption.

3.2 DATA-DRIVEN APPROACH

The data-driven approach makes use of increasing building data availability. The real-world data are usually in the form of time series, e.g., in hourly resolution. In the first step, traditional (statistical) methods, such as regression analyses or modern machine learning methods, may be used when buildings are segmented into archetypes.

These modern methods range from clustering algorithms and neural networks to decision trees. Furthermore, these algorithms are also very effective and suitable in the second phase of characterizing archetypal parameters since they can capture complex nonlinear relations amongst data. Finally, in the third step of calibrating these parameters, typically statistical methods are used, particularly maximum likelihood estimation or, in general, approaches based on Bayesian inference.

3.2.1 BAYESIAN PARAMETER CALIBRATION

First, assume a building model with an energy model G, then the relation between the observed data y and simulated energy data can be described as

$$y = G(x, w, \theta) + \varepsilon, \tag{1}$$

where x is a vector of fixed (low-uncertainty) parameters and θ is a vector of unknown (high-uncertainty) parameters to be found. The vector of weather measurements is denoted as w and $\varepsilon \sim N(0, \sigma^2)$ is a residual error term that is supposed to be independent and identical (i.i.d.) Gaussian distributed.

In a Bayesian context, the true, i.e., calibrated, parameter distributions after seeing the data are referred to as posterior distributions following the Bayes theorem. The posterior probability density of the parameters of this model is then given by

$$p(\theta|y) \propto p(\theta)p(y|\theta), \tag{2}$$

where $p(\theta|y)$ is the joint posterior density of the archetype-level parameters conditional on the data, $p(y|\theta)$ is the joint data likelihood conditional on the model G and parameters, and $p(\theta)$ is the joint prior density of the archetype-level parameters.

3.2.2 BUILDING ENERGY MODEL

The crucial part when calibrating the desired parameters comes when the energy model G is to be defined. There are two fundamental types of models to be considered for ABEMs – static and dynamic. The choice depends on many factors; however, a static model may generally be sufficient if the primary goal is to estimate total daily energy use. Neglecting the dynamic behavior of the building construction is possible due to low time resolution, which brings the benefit of being less computationally intensive.

For instance, such a model can describe the heating load curve, i.e., the dependency of the building heating load on the weather. The model is basically a particular type of sigmoid – the Gompertz curve:

$$\phi = A\exp[-\exp(-C(T_{out} - Q))], \tag{3}$$

where ϕ is the heating load, T_{out} is the outdoor temperature, and the triple $\{A, C, Q\}$ are the parameters that shape the Gompertz curve. For more detail, including the model parameter calibration, the reader is referred to [11].

As aforementioned, the ABEM can also be dynamic, especially when hourly energy use estimates are needed. Typically, the building model for space heating is simplified, assuming only one zone. The thermal inertia of the building is accounted for by modeling thermal resistances and the adequate thermal capacity, as well as the internal and solar heat gains in an equivalent *x*-node resistance-capacitance network. These building (RC network) models are very well-known, and their detailed description can be found in [12] or further in this document in Section 8.2.3.

4   LOW-ORDER MODELS FOR DISTRICT HEATING

District heating is a system that provides space and water heating to multiple buildings from a central plant. The heat generated in this plant is delivered to consumers via an insulated double-pipeline system. Hot water is transported through the forward pipe to the buildings, where it releases its heat. The cooled water returns to the plant through the return pipe to be reheated, ensuring a continuous hot water supply. Therefore, a district heating system comprises three primary components: central heat-producing units, a distribution network, and consumer installations for space heating and hot water production. The central units generate heat, which is then transported via the distribution network to the consumer installations, where it is utilized for heating spaces and providing hot tap water [13].

Consider a simple district heating network comprising a single consumer and one plant. Ignoring diffusion, the time delay, $\tau(t)$, of a water particle leaving the plant at a time t is related to the distance d between the plant and consumer, governed by the equation [14]

$$d = \int_0^{t+\tau(t)} v(s)\,\mathrm{d}s \tag{4}$$

where $v(s)$ is the velocity of the particle at a time s. A simplified district heating system is demonstrated in Fig. 2. In this figure, the temperature of the district heating plant and the end user are denoted as T_s and T_n, respectively.
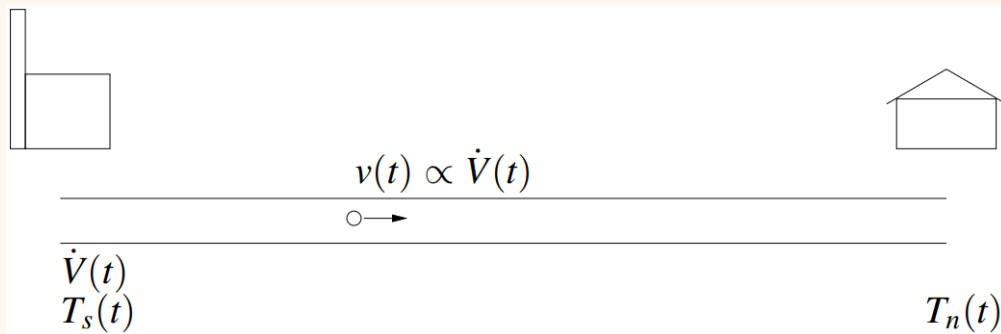

Fig. 2 Simplified district heating system.

This model shows that the flow needs to be filtered by averaging past values but with a varying horizon. In practice, this is achieved by assuming a known volume for the district heating pipe between the plant and the consumer.

The network temperature in a district heating system is modeled by [15]

$$y_t = \sum_{i \in L_y} a_i(x_{t-m})y_{t-i} + \sum_{i \in L_u} b_i(x_{t-m})u_{t-i} + e_t, \tag{5}$$

where t is the time index, y_t is the response, x_t and u_t are inputs, e_t is i.i.d. $N(0, \sigma^2)$, L_y and L_u are sets of positive integers defining the autoregressive and input lags in the model, and m is a positive integer. Finally, $a_i(\cdot)$ and $b_i(\cdot)$ are unknown but smooth functions that are to be estimated.

4.1 CONDITIONAL PARAMETRIC ARX-MODELS

The model represented by the equation (5) can be written in a compact form as follows:

$$y_t = z_t^T \theta(x_t) + e_t, \tag{6}$$

where the observations of the response are denoted as y_t and the explanatory variables are x_t and z_t exist for observation numbers $t = 1, \dots, n$. Moreover, e_t is i.i.d. $N(0, \sigma^2)$ and $\theta(\cdot)$ is a vector of coefficient functions to be estimated.

Let $\theta_j(.)$ be the jth element of $\theta(.)$, and let $p_d(x)$ be a column vector of terms in d-order polynomial kernel functions evaluated at x. For instance, if $x = [x_1, x_2]^T$, then $p_2(x) = [1, x_1, x_2, x_1^2, x_1 x_2, x_2^2]^T$. Furthermore, let $z_t = [z_{1t}, \dots, z_{pt}]^T$, then with

$$u_t^T = \left[z_{1t} p_d^T(1)(x_t), \dots, z_{jt} p_d^T(j)(x_t), \dots, z_{pt} p_d^T(p)(x_t) \right] \tag{7}$$

And

$$\phi^T = \left[\phi_1^T, \dots, \phi_j^T, \dots, \phi_p^T \right], \tag{8}$$

where $\phi_j(x)$ is a column vector of local coefficients at x corresponding to $z_{jt} p_d^T(j)(x_t)$. The linear model

$$y_t = u_t^T \phi + e_t, \quad t = 1, \dots, N, \tag{9}$$

Is then fitted locally using weighted least squares (WLS) as

$$\hat{\phi}(x) = \arg \min_{\phi} \sum_{t=1}^{N} w(x)(y_t - u_t^T \phi)^2, \tag{10}$$

for which a unique closed-form solution exists provided the matrix with rows u_t^T corresponding to non-zero weights have full rank. The weights are assigned as

$$w_t(x) = W \left(\frac{\|x_t - x\|}{h(x)} \right), \tag{11}$$

where $W(.)$ is a nowhere-increasing weighting function, $\|.\|$ denotes the Euclidean norm, x denotes a single point within the range of the observations $x_t; t = 1, \dots, N$, and $h(.)$ is the bandwidth used for the particular fitting point. If $h(x)$ is constant for all values of x, it is denoted as a fixed bandwidth. If h is chosen so that a certain fraction (α) of the observations (x_t) is within the bandwidth, it is denoted as nearest neighbor bandwidth. As an example,

$$W(x) = \begin{cases} (1 - x^3)^3, & x \in [0; 1) \\ 0, & x \in [1; \infty), \end{cases} \qquad (12)$$

can be used, which provides weights between 0 and 1.

Considering

$$\hat{\phi}^T(x) = \left[\hat{\phi}_1^{\;T}(x), \dots, \hat{\phi}_j^{\;T}(x), \dots, \hat{\phi}_p^{\;T}(x) \right], \qquad (13)$$

where $\hat{\phi}_j(x)$ is a column vector of local constant estimates of ϕ at x corresponding to $z_{jt} p_d^T(j)(x_t)$. The estimation θ values are handled by fitting the linear model

$$\hat{\theta}_j(x) = p_d^T(j)(x)\hat{\phi}_j^{\;T}(x), \quad j = 1, \dots, p. \qquad (14)$$

Note that if $z_t = 1$ for all t, the method of estimation reduces to determining the scalar $\hat{\theta}(x)$ so that $\sum_{t=1}^{N} w_t(x) \left(y_t - \hat{\theta}(x) \right)^2$ is minimized, i.e. the method reduces to kernel estimation.

4.2 APPLICATION AND RESULTS

This section illustrates the application of the method to data obtained from the district heating plant "Høje Taastrup Fjernvarme" near Copenhagen in Denmark. For the periods considered, the energy was supplied from only one plant. Data consists of five-minute samples of supply temperature and flow at the plant together with the network temperature at a major consumer, consisting of 84 households.

Below results corresponding to two different model structures are presented, 1) the *non-linear Finite Impulse Response (FIR) model*

$$Y_t = \sum_{i=0}^{30} b_i(X_t)U_{t-i} + \epsilon_t, \qquad (15)$$

and 2) the *non-linear ARX-model*

$$Y_t = a(X_t)Y_{t-1} + \sum_{i=3}^{15} b_i(X_t)U_{t-i} + \epsilon_t, \qquad (16)$$

where Y_t represents the network temperature, U_t represents the supply temperature, and X_t represents a filtered value of the flow [16].

Local quadratic estimates and nearest neighbor bandwidths are used for the FIR and ARX models described in the previous section. In Fig. Fig. 3 the impulse response as a function of the flow is displayed for $\alpha = 0.4$. Equivalent plots for the remaining bandwidths revealed that for $\alpha \leq 0.2$ the fits are too noisy, whereas in all cases, sufficient smoothness is obtained at $\alpha = 0.5$. Only minor differences in the fits are observed for $\alpha \in \{0.3, 0.4, 0.5\}$.
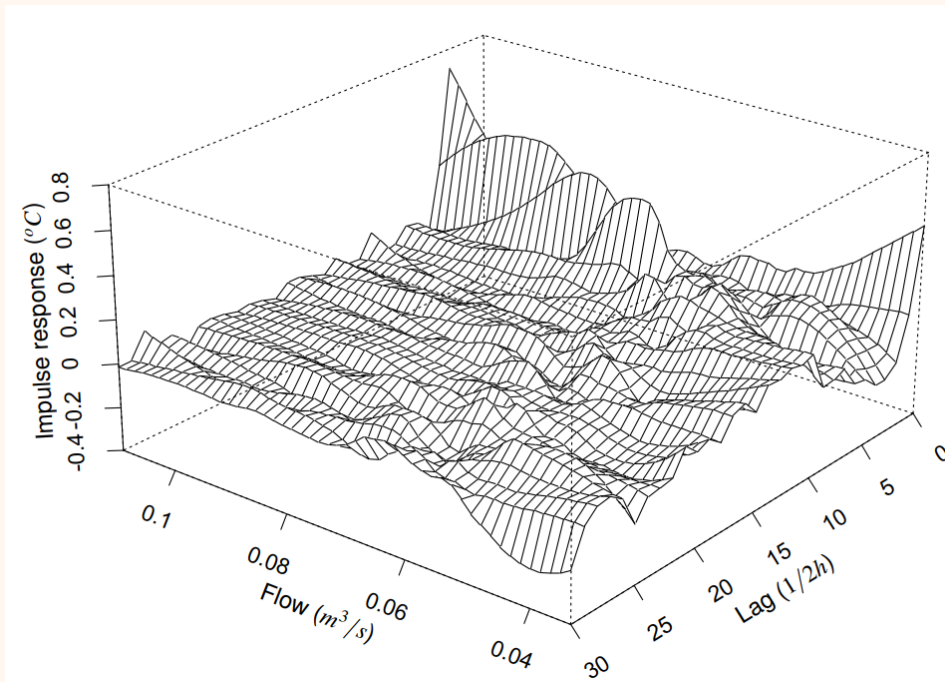
Fig. 3 Impulse response of the FIR model.

In Fig. 4 a contour plot corresponding to Fig. 3 is shown. The contour lines are plotted from -0.1 to 0.7 °C in steps of 0.1 °C, lines corresponding to non-positive values are dotted. From the plot, the varying time delay of the system is revealed; it seems to vary from three lags when the flow is large to approximately ten lags when the flow is near its minimum.
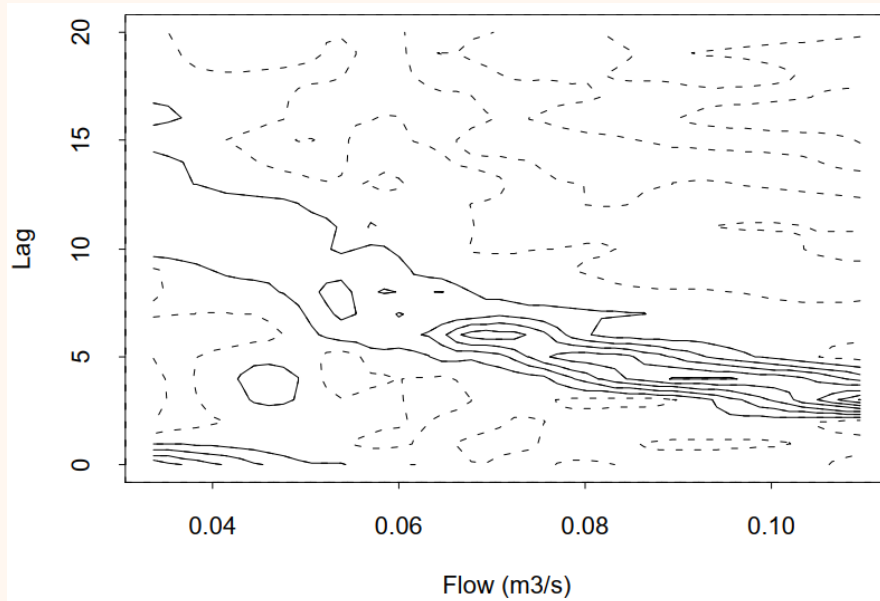

Fig. 4 Contour plot of the impulse response of the FIR model.

For $\alpha = 0.4$ the impulse response of the ARX model as a function of the flow is displayed in Fig. 5. The varying time delay is clearly revealed.
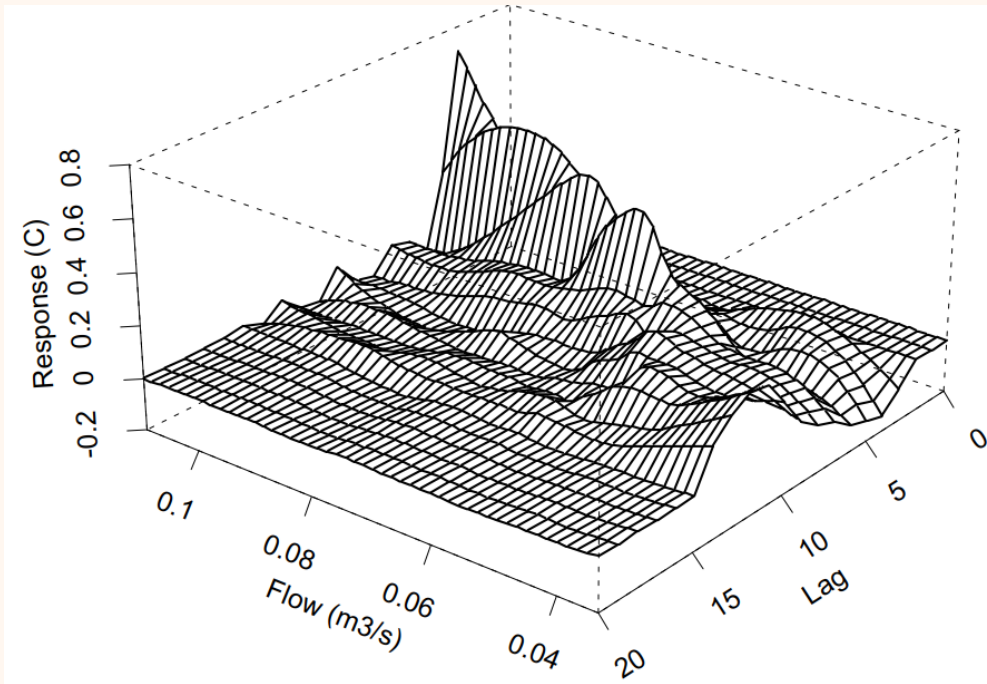
Fig. 5 Impulse response of the ARX model.

The stationary gain of the two models and the pole of the ARX model are shown in Fig. 6. The model describes the relation between the temperature at the plant and the network temperature. Hence, in the case of no temperature loss, the stationary gain (the stationary gain for constant flow) must be 1. From the estimated values of the stationary gain it is seen that the temperature loss changes from 6 % when the flow is large to 12-15 % when the flow is small. This clearly illustrates that no single values exist for the stationary gain as for the linear models; in the considered case, the stationary gain and the location of the pole depend on the flow.
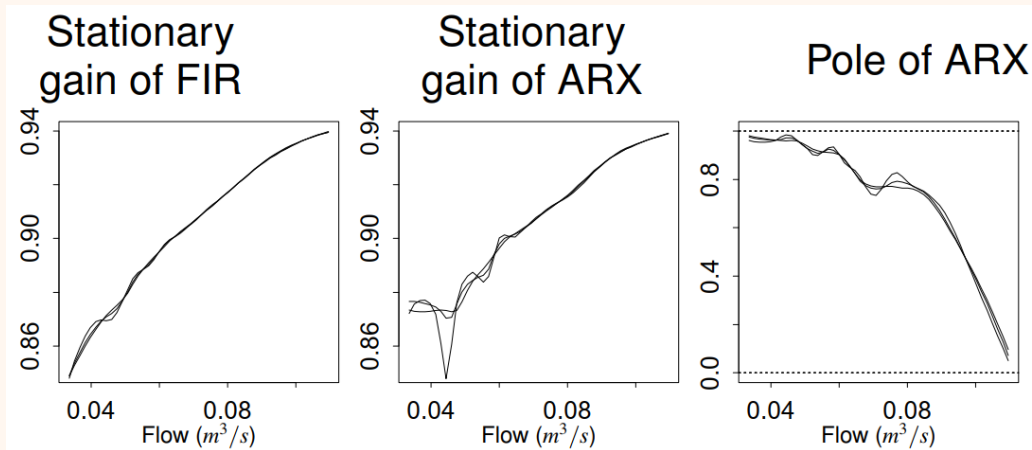

Fig. 6 The stationary gain of the FIR model (left) and ARX model (middle), and the pole of the ARX model (right) are all plotted against the flow and for NN bandwidth α equal to 0.3, 0.4, and 0.5.

5 MODELS FOR LONG-TERM STORAGE TO SUPPLY A DISTRICT (TRENTO DEMO)

The Trento demonstration project implements the thermal activation of two existing tunnels which are currently used as a museum. The tunnels were part of the Italian roadway network, but after the construction of a new tunnel in 2007, they fell into disuse, being partly transformed into a museum one year later. The tunnels are located in the district of Piedicastello, a part of the city of Trento, and cross a 100 m high spur of limestone called Doss Trento.

A potential solution for thermally activating the Piedicastello tunnels is to exploit the Doss 100-meter depth by drilling and placing radial borehole heat exchangers (rBHEs) at various cross sections within the more internal part of the tunnel. Fig. 7(a) shows a 3D view of the rBHEs solution. This solution preserves the visibility of the lining's inner surface, thus not affecting future inspections while remaining largely unaffected by the tunnel's internal air temperature and humidity conditions.
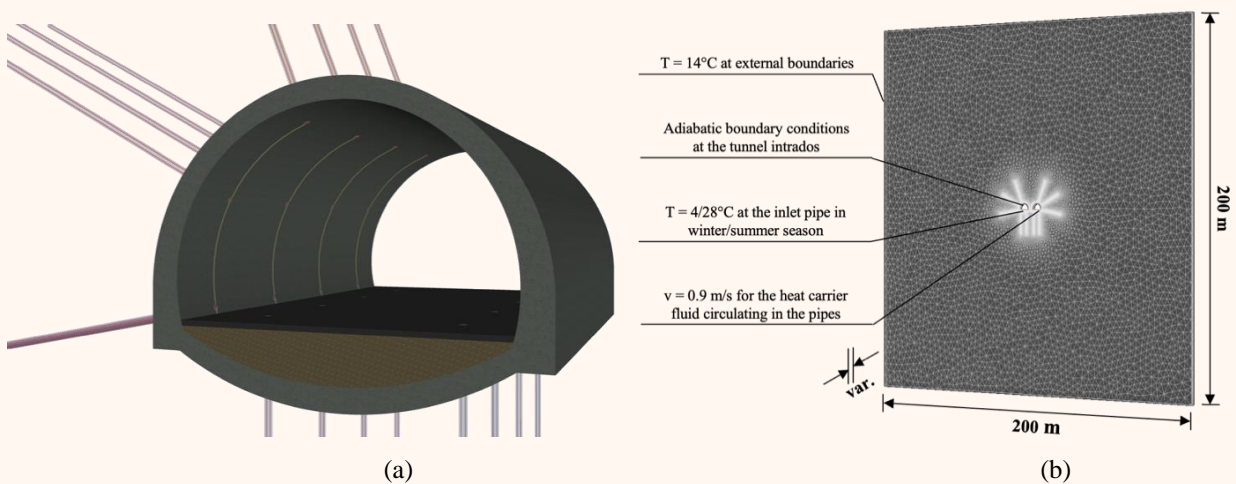

(a)   (b)

Fig. 7 (a) 3D view of the thermal activation solution and (b) numerical model.

5.1 MODELLING

A 3D numerical model was built with the Finite Element software Feflow to assess the thermal performance of the tunnels. The model has dimensions of 200 m in height and width, with a thickness that fluctuates based on the spacing between the rBHE cross-sections Fig. 7(b). The Piedicastello tunnel consists of two horseshoe-shaped tubes, each with an equivalent external diameter of 12.7 m and a concrete lining ranging from 80 to 130 cm thick. Conversely, the heat exchanger pipes were simplified to one-dimensional elements ("discrete features") in the model, having a cross-sectional area of 201 mm^2, equivalent to an external diameter of 20 mm and a thickness of 2 mm.

The velocity of the fluid in the pipes is equal to 0.9 m/s. The speed was assumed by considering the results of an optimization study as well as insights from previous on-site operations [13–15]. The fluid considered was plain water. Nevertheless, water-glycol mixtures may be used for the final application, too. The volumetric flow rate in each pipe ($\dot{m}$) is thus equal to 0.65 m^3/h.

Inlet temperatures assumed constant, are typical values that were found in the literature [15–18] and which are representative of the functioning of these systems.

Simplified assumptions were established for both thermal and hydraulic boundary conditions. That was due to insufficient data on the Doss Trento groundwater conditions and the internal air environment in the Piedicastello tunnels during the evaluation. By neglecting the potential impacts of these factors (i.e., applying adiabatic conditions to the tunnel boundary and modeling a dry rock mass), a preliminary sensitivity analysis was conducted to gain initial insights into critical design parameters for the rBHE system.

To achieve this, three borehole length configurations (short: 12.50 m, medium: 18.75 m, long: 25.00 m) and three cross-sectional spacing distances (3.0 m, 5.0 m, and 7.5 m) were examined.

The following equations represent the thermal power and energy exchanged by the rBHEs system:

$$P = \dot{m}\, \rho\, c_s\, (T_{out} - T_{in}) \tag{17}$$

$$Q_h = P_h\, Nd_h\, h_h \tag{18}$$

$$Q_c = P_c\, Nd_c\, h_c \tag{19}$$

Positive values represent energy absorbed from the ground, while negative values represent thermal energy charging of the Doss. Tab. 1 describes the parameters used in the Equations (17)–(19).

Tab. 1 Parameters used in Equations (17)–(19).

Name	Symbol	Unit	Reference value
Power exchanged	P	kW	-
Energy exchanged during the heating period	Q_h	kWh	-
Energy exchanged during the cooling period	Q_c	kWh	-
Days of operation of the heating system	Nd_h	Days	180
Hours of operation of the heating system	h_h	Hours/day	14
Days of operation of the cooling system	Nd_c	Days	90
Hours of operation of the cooling system	h_c	Hours/day	10
Volumetric flow rate	$\dot{m}$	m³/h	0.65
Density	ρ	kg/m³	1000
Specific heat	c_s	kJ/kg K	4.20
Inlet temperature (heating)	T_{in}	°C	4 °C
Inlet temperature (cooling)	T_{in}	°C	28 °C
Outlet temperature	T_{out}	°C	-

5.1.1 LONG-TERM ENERGY STORAGE

The Drake Landing Solar Community in Okotoks, Canada, is one of the first examples of a real implementation of long-term energy storage in the ground through borehole heat exchangers. However, also in Europe, a rising number of borehole thermal energy storage systems has recently been experimented. The existing examples mainly rely on storing industrial waste heat, cogeneration heat surplus, or heat from solar thermal systems.

From a long-term perspective, if used to store the excess heat produced in summer to exploit it in winter, the borehole heat exchangers can cause a significant increase in the ground temperature.

Some scientific applications have recently tried to evaluate the potential of thermal energy recharge and discharge of the ground during summer and winter periods due to the implementation of geothermal heat pumps. Today, borehole thermal energy storage can also be used for combined heating and cooling purposes. Typical applications regard high-insulated office buildings that, due to their efficient heat retention, often necessitate cooling solutions to offset the thermal load generated by internal operations, particularly in summer. This recovered heat energy is delivered to the ground to be conserved for heating buildings during winter months.

The Piedicastello case study represents a peculiar situation in which there is no availability of industrial waste heat or solar thermal heat in surplus to be stored in the Doss Trento inner bedrock. However, the new geothermal heat pump system could exchange a significant amount of heat with the Doss, resulting in a detrimental effect over time if the heat stored in the rocks is not recharged. Thus, the ideal operational strategy foresees the storage of the heat dissipated in summer by the rBHEs in the ground coupled with the absorption of the thermal energy from the geothermal source in the winter operational mode.

The solution was initially conceived to provide energy to a new low-energy district in Piedicastello: buildings with a high level of insulation and roughly equal heating and cooling requirements (e.g., office or commercial spaces) were supposed for the evaluation of the long-term storage.

By the way, the possibility of reducing the initial storage of the geothermal energy in the long term due to a higher heating energy requirement in comparison with the cooling one was also checked with a seasonal focus (see Equation (20)).

The energy conservation principle was considered to model the long-term heat storage in the Doss Trento:

$$\Delta Q_{st} = \sum_{d=1}^{Nd_h} Q_{h,d} + \sum_{d=1}^{Nd_c} Q_{c,d},\tag{20}$$

where Q_d is the thermal energy exchanged by the boreholes at a day d determined using (18)–(19) and ΔQ_{st} is the variation of the thermal energy stored in the Doss bedrock concerning the situation without energy activation of the tunnels.

5.2 A CASE STUDY: RESULTS

The results of the preliminary numerical simulations performed are presented in Tab. 2. Within the examined parameters, the outcomes of the analysis indicate that:

- longer rBHEs yield higher heat extraction, necessitating a balance between heat recovery and the associated costs of pumping and drilling to determine optimal borehole length.
- there is negligible interaction between adjacent instrumented cross-sections when their spacing exceeds 5.0 meters.

Tab. 2 Computed input/output temperature difference in winter and summer seasons after 30 days of operation.

		Winter			Summer		
		3.0 m interaxis	5.0 m interaxis	7.5 m interaxis	3.0 m interaxis	5.0 m interaxis	7.5 m interaxis
Short	5 × 12.50 m	2.12 °C	2.26 °C	2.28 °C*	2.96 °C	3.16 °C	3.19 °C*
Mid	5 × 18.75 m	3.00 °C	3.18 °C	3.20 °C	4.19 °C	4.45 °C	4.49 °C
Long	5 × 25.00 m	3.78 °C	3.99 °C	4.02 °C	5.29 °C	5.59 °C	5.63 °C

*Analyses run in the long term as well

The first solution (5x12.5x7.5 m) provides a power exchange after 30 days of operation equal to 1.72 kW in winter and -2.41 kW in summer. The scenario with rBHEs length 18.75 m and sections distanced 7.5 m provides a power exchange after 30 days of operation equal to 2.43 kW in winter and -3.40 kW in summer. Considering the scenario with long boreholes placed in cross sections distanced 7.5 m, the power exchanged after 30 days of operation equals 3.04 kW in winter and -4.26 kW in summer.

In addition to the analyses shown above, the case of short configuration with 7.5 m interaxis (whose results are marked with an asterisk in Tab. 2) was run for three years, considering a continuous winter operation for around 180 days and a continuous summer operation for around 90 days. The thermal field obtained at the end of winter and summer season during the third year of operation is depicted in Fig. 8.
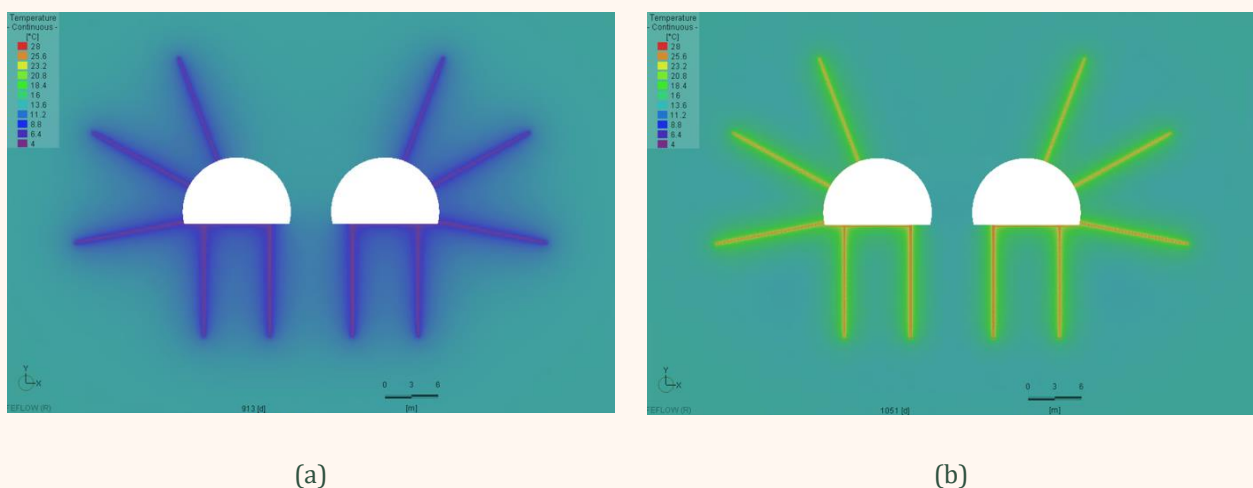

(a)   (b)

Fig. 8 Thermal field at the end of (a) winter and (b) summer season during the third year of operation.

Fig. 9 shows that in the third year, the temperature difference in winter is 1.79 °C, while it is -3.12 °C in summer. Additionally, depending on whether the analysis starts from winter or from summer operation the results differ slightly, especially in the first two years. An initial winter operation guarantees a thermal reservoir in the rock mass surrounding the tunnel, which is more prone to store heat the following summer. An initial summer operation provides more favorable results in heat extraction in winter.
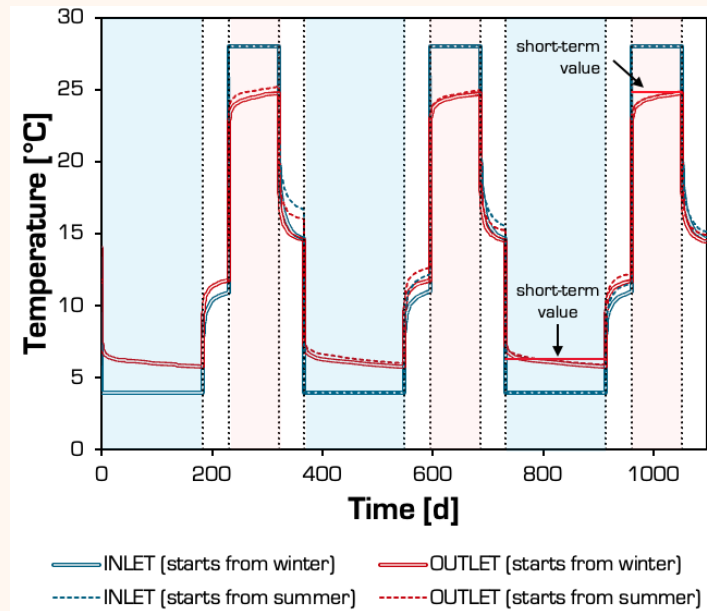

Fig. 9 Computed output temperature difference in winter and summer seasons over 3 years of operation and comparison with short-term results (5x12.5x7.5 m).

These results show that the temperature difference obtained in summer after 30 days of operation is reasonable also in the long term. However, that obtained in winter must be taken cautiously since it would further decrease after around 1.5 months of operation. It must be kept in mind that the hypothesis of continuous operation provides a lower-bound solution in this regard. For this reason, the following results will be considered for the analyses over 30 days.

The solution with the shortest length of the rBHEs is the best for long-term storage balance under the assumed hypotheses.

- The overall thermal energy discharged from the Doss storage in winter equals 4.36 MWh.
- The overall thermal energy charged into the Doss storage in summer equals -2.18 MWh.
- Thus, every year, about 2.18 MWh are not balanced into the Doss thermal energy storage with a possible decrease in the system's performance. The geothermal reservoir could partially recharge naturally over the remaining 95 days/year.

Considering a very low-energy building characterized by a low-temperature heating and cooling system with 35 kWh/m2y as the thermal energy requirement for heating and 24 kWh/m^2y for cooling, only one section of the geothermal solution proposed is expected to cover the thermal energy demand of roughly 115 m^2.

6 MODELS FOR CENTRALIZED HVAC IN APARTMENT BUILDINGS (PALMA DEMO)

In the Palma demo, several innovations are being developed. One of them is the advanced control of heat pumps for centralized DHW production. This innovation will be deployed in Palma demo's new high-efficiency residential multifamily building. This building has centralized heat pumps to produce DHW and two water tanks to store it. The building also has a PV installation for common building consumptions such as heat pumps.

Thus, for the advanced control of the installations, it is necessary to generate models of the heat pumps, the storage tanks, and the PV.

6.1 THERMAL COMPONENTS

A general overview of the thermal systems models is represented in Fig. 10. Each part of the model will then be described in detail hereafter. In the schematic, the model's parameters are represented in blue, the variable states in black, the exogenous non-controllable inputs in green, and the controllable inputs in red.
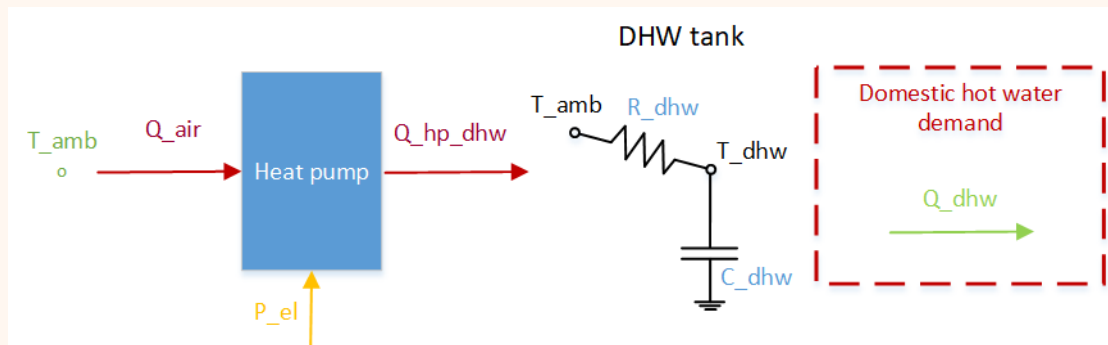

Fig. 10 General scheme of the thermal part of the centralized heat pump for DHW production.

6.1.1 STORAGE TANKS

The system includes two thermal storage tanks for DHW. They have the same capacity (1500 liters) and insulation and are connected in series, one being at a 5 K higher temperature than the other. For modeling, they were considered as a single tank.
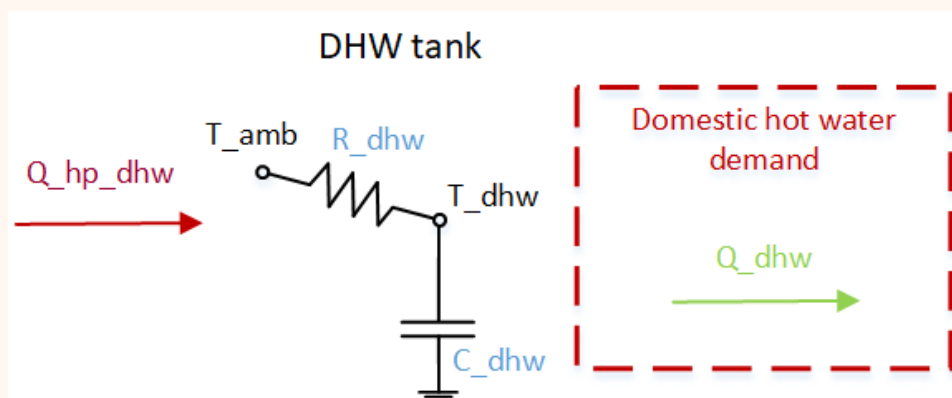

Fig. 11 RC scheme of the one-node model for the storage tanks.

Fig. 11 represents the RC model of the tank where:

- C_{dhw}: thermal capacity of the whole tank [kWh/K]
- R_{dhw}: resistance of thermal losses through the envelope of the tank [K/kW]
- $Q_{hp_{dhw}}$: thermal power of charging by the HP [kW]
- Q_{dhw}: thermal power of DHW consumption [kW]
- T_{amb}: temperature of the surrounding environment [°C]
- $T_{hp_{in}}$ and $T_{hp_{out}}$: temperature of the water entering and leaving the heat pump [°C]
- $T_{dhw_{out}}$ and T_{mains}: temperature of the DHW consumption and water mains, respectively [°C]

Equation (21) represents the dynamic behaviors of the node's temperatures. Equations (22) and (23) describe the heat flows

$$C_{dhw}\dot{T}_{dhw} = \frac{1}{R_{dhw}}(T_{amb} - T_{dhw}) - Q_{dhw} + Q_{hp_{dhw}}, \qquad (21)$$

$$Q_{hp_{dhw}} = m_{hp}\, cp_{water}(T_{hp,out} - T_{hp_{in}}), \qquad (22)$$

$$Q_{dhw} = m_{dhw}cp_{water}(T_{dhw_{out}} - T_{mains}), \qquad (23)$$

Tab. 3 describes all the different parameters that are part of the storage tank model.

Tab. 3 Variables of the DHW tank model.

Name	Type	Symbol	Units	Example value
Parameters				
Capacitance of the tank	float	C_{dhw}	kWh/K	3.49
Thermal resistance of the tank	float	R_{dhw}	K/kW	182.9
Water specific heat	float	cp_{water}	Wh/kg·K	1.163
Inputs				
Ambient temperature	float	T_{amb}	°C	20
Inlet temperature from DHW circuit	float	$T_{hp_{in}}$	°C	35
Outlet temperature from DHW circuit	float	$T_{hp_{out}}$	°C	30
Supply temperature of the DHW production	float	$T_{dhw_{out}}$	°C	40
Mains water temperature	float	T_{mains}	°C	11

Name	Type	Symbol	Units	Example value
Inputs				
Water flow from the hp to the tanks	float	$\dot{m}_{hp}$	kg/s	0.05
Water flow from the tanks to the households	float	$\dot{m}_{dhw}$	kg/s	0.05
Heat provided by the heat pump	float	Q_{hp}	kW	-
Heat consumed by the DHW consumption	float	Q_{dhw}	kW	-

6.1.2 HEAT PUMP

The heat pump behavior is represented by a model of two equations that calculate its efficiency (the COP – the Coefficient of Performance) and maximum capacity. COP (the ratio between the heat produced and the electrical consumption) is a simplified model that only depends on the ambient and supply temperatures. Equation (24) shows how the inverse of the COP is calculated.
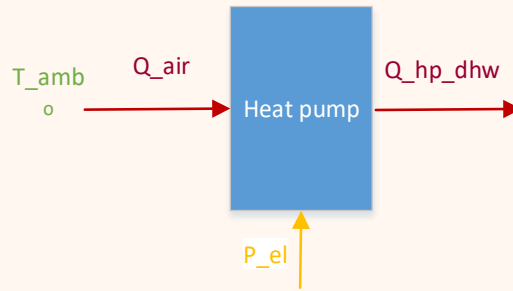

Fig. 12 Scheme of the heat pump model.

$$\frac{1}{COP} = \frac{P_{el}}{Q_{th}} = a_0 + a_1 T_{amb} + a_2 T_{sup},$$
(24)

Tab. 4 shows the variables that are included in the heat pump model.

Tab. 4 Variables of the heat pump model.

Name	Type	Symbol	Units	Example value
Parameters				
COP model coefficient	float	COP_{a0}	-	0.14385
COP model coefficient	float	COP_{a1}	K^{-1}	-0.00467
COP model coefficient	float	COP_{a2}	K^{-1}	0.00503
Max. capacity model coefficient	float	Q_{b0}	kW	34.34979
Max. capacity model coefficient	float	Q_{b1}	kW/K	0.35831
Max. capacity model coefficient	float	Q_{b2}	kW/K^2	-0.00609

Name	Type	Symbol	Units	Example value
Inputs				
Ambient temperature	float	T_{amb}	°C	10
Supply temperature	float	T_{sup}	°C	45
Outputs				
Heat pump COP	float	COP	-	3.45
Heat pump maximum capacity	float	Q_{max}	kW	10.6

The maximum capacity of a heat pump is linked with the ambient temperature: in cold environments, the capacity is reduced. Equation (25) shows the quadratic model of the maximum capacity heat pump.

$$Q_{max} = b_0 + b_1 T_{amb} + b_2 T_{amb}^2 \tag{25}$$

6.2 ELECTRIC COMPONENTS

PV production is forecasted to be included in the optimization problem. Self-consumption and the imports from the grid had to be considered. The production is obtained by following the mathematical model of Huld et al. [23] which relates the power generated to solar irradiation and nominal and relative efficiencies. Equation (26) shows the mathematical model:

$$P = G \cdot A \cdot \text{eff}(G, T_m) = G \cdot A \cdot \text{eff}_{nom} \cdot \text{eff}_{rel}(G', T'_m) \tag{26}$$

where G is solar irradiation on the surface panel, A is a PV area and eff_{nom} is the nominal efficiency of the module. The relative efficiency eff_{rel} depends on the module material and environmental conditions such as temperature and wind speed.

$$eff_{rel}(G', T'_m) = 1 + k_1 \ln(G') + k_2 \ln(G')^2 + k_3 T'_m + k_4 T'_m \ln(G') + \\ + k_5 T'_m \ln(G')^2 + k_6 T'^2_m \tag{27}$$

$$T_m = T_a + \frac{G}{U_0 + U_1 W} \tag{28}$$

$$G' = \frac{G}{1000} \text{ and } T'_m = T_m - 25 \tag{29}$$

The wind speed and the temperature are obtained from weather forecast services. The solar irradiation as well, although it is transformed to calculate the actual incident radiation on the plane of the panels, considering their orientation and inclination.

7 PV FORECASTING AND MODELING PV-BATTERY SYSTEM (KARVINÁ AND UTRECHT DEMOS)

7.1 KARVINÁ DEMO

Karviná's demo PV power source consists of a roof PV system (BAPV) of almost 30 kWp and a facade PV system (BIPV) of 5kWp. Also, there are PV thermal collectors that can provide 5.7 kWp in electricity and 15.7 kW in thermal. The system is backed by a battery with a total capacity of 50 kWh, delivering 30 kW of power at a time. To enable predictive energy management, a weather station with additional sensors and a sky-imager was installed in advance at a nearby building. This provides us with the advantage of historical data from the site that was partially used to help estimate dimensions of the system in connection with intelligent model predictive control (MPC) of the building according to external dynamic price signals (day-ahead market).

7.1.1 PV FORECASTING

Since October 2022, a weather station with a sky-imager and irradiance sensor was installed near the demo site to capture local weather characteristics, which are later used for numerical models to learn from the data.

Fig. 13 The weather station setup includes a sky-imager and a reference solar irradiation sensor.

Weather station and irradiance sensor setup collects:

- solar irradiance [W/m2],
- temperature (PV module temp., ambient),
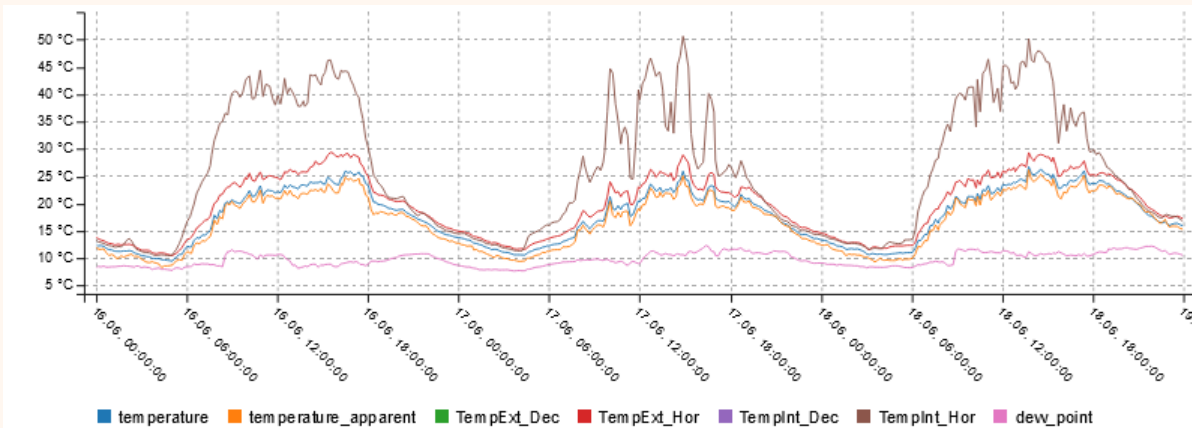- wind characteristics, air humidity, atmospheric pressure, and precipitation.

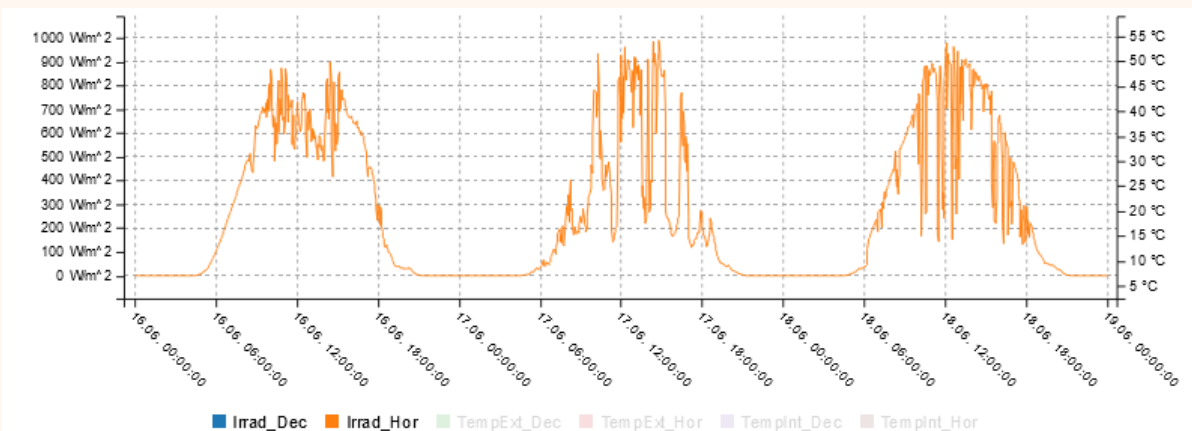*Fig. 14 Monitored temperature data by the weather station.*

Fig. 15 Monitored data from the reference irradiance sensor.

PV Forecast runs as a software-as-service (SaaS) and relies on external numerical and satellite-based predictions. A numerical prediction that provides an irradiation forecast of a rough time and space resolution is commonly available. Therefore, source predictions have to be interpolated using the spline method [24]. A way to further improve interpolated forecast accuracy is to use locally measured data as feedback to correct the general forecast of irradiation.

PV Forecast incorporates forecasting using statistical models and nowcasting using persistent models and sky-imaging.

Statistical model

A statistical model has been implemented as other conditions were expected to deviate systematically at a given place. The concept is to compare locally measured values to predicted irradiation values at a particular historical period – a learning period. This correction is then applied to future forecasted values.
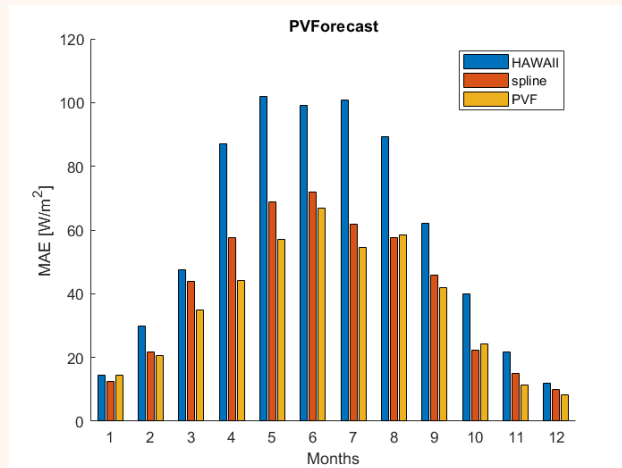
Fig. 16 Monthly overview of numerical and statistical model errors. The HAWAII model is used as an external numerical prediction interpolated using a spline and then corrected by PVForecast.

Persistent model

There are at least two approaches to improve irradiation forecasting accuracy further using the persistent model. Both use irradiance measurement sensors that give the model feedback in real time. Next, a correction is calculated and applied to a short-time prediction horizon. The persistence of recent weather conditions is not expected to overlap days. Hence, the correction of the prediction horizon was set to 8 hours. Fig. 17 shows the error comparison of the following persistent models.

The *nowcast model* compares measured feedback to the theoretical maximum irradiation (Nowcast theory).

$$G_{T_2}^{Nowcast} = G_{T_2}^{theor} \frac{G_{T_1}^{meas}}{G_{T_1}^{theor}} \tag{30}$$

The *combined model* compares measured feedback to predicted irradiation (Nowcast PVF)

$$G_{T_2}^{Combined} = G_{T_2}^{PVF} \frac{G_{T_1}^{meas}}{G_{T_1}^{PVF}} \tag{31}$$

where G^{theor} is theoretical maximal irradiance, G^{meas} is recently measured irradiance, G^{PVF} is original forecasted irradiance, T_1 is recent time and T_2 is forecasted horizon time.
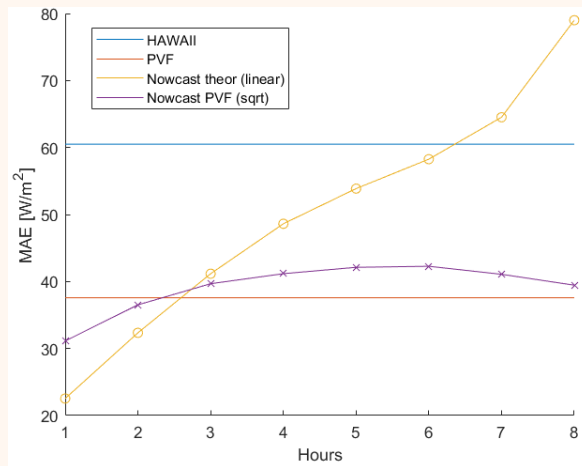
Fig. 17 Persistent models comparison to statistical (PVF) and numerical (HAWAII). Error progress with increasing future prediction interval.

The main advantage of the nowcast using a persistent model is high precision in a very short time horizon of 1 or 2 hours since the weather changes slowly. On the other hand, the error significantly increases with a longer prediction horizon.

The influence of the correction is decreased for future prediction values by the weight function. A linear weight is used for the Nowcast, and square root function-based weights are used for the model, combining both statistical and persistent models. The combined model is recalculated hourly as soon as the new feedback from measurement sensors is available. This means that the future irradiance curve gets updated regularly every hour.
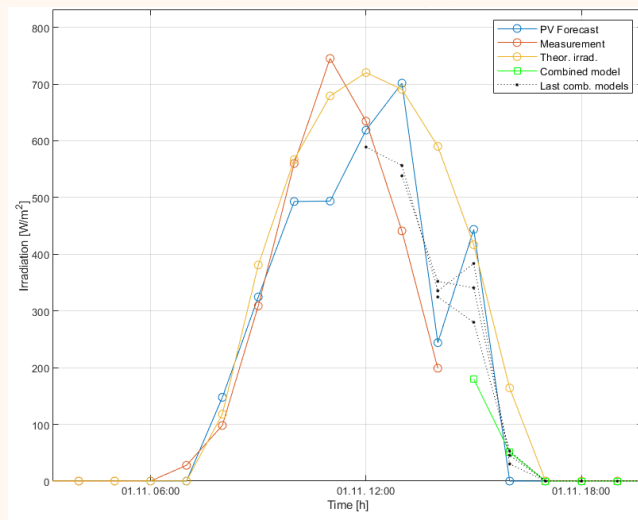

Fig. 18 Persistent models comparison to statistical (PVF) and numerical (HAWAII). Error progress with increasing future prediction interval. The previously calculated models are displayed in black to show the progress of constant improvement.

Cloud tracking

Specialized sky imaging hardware and software are needed for short-time prediction with high accuracy. Local all-sky images are taken in short-time intervals of around 10 seconds and processed.
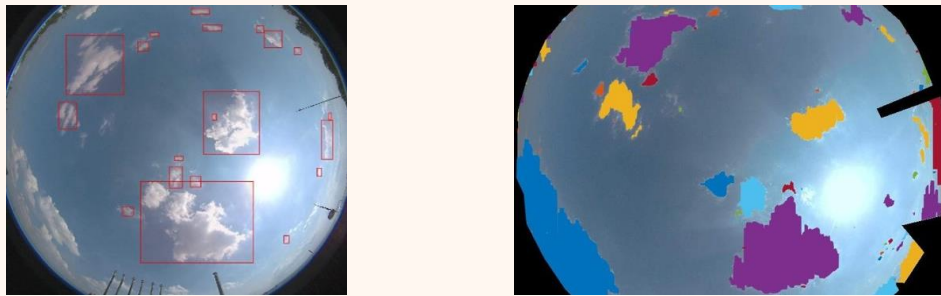
Fig. 19 The intermediate result of the cloud tracking procedure is cloud tracking (left) and color segmentation (right).

Despite this procedure being computationally demanding, it brings the best results for the very near future (up to a 20-minute horizon) with a minimum time step of one-minute resolution. A low RMSE exhibits good timeliness of irradiation drop prediction.
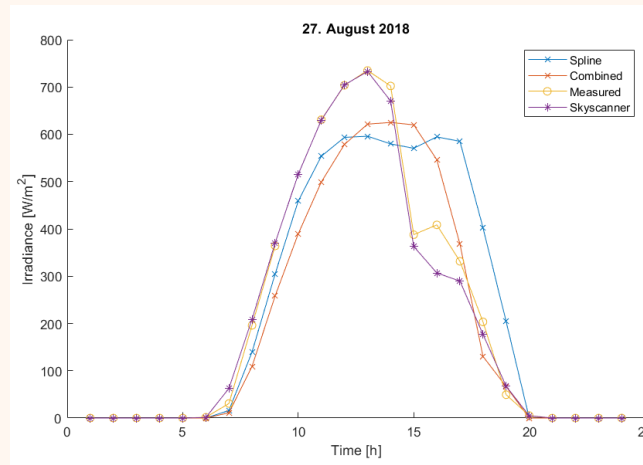

Fig. 20 Irradiance forecast comparison to measured samples.

A cutting-edge technology of sky imaging can assert intraday energy trading and balancing grid demands. Nowadays, it is crucial to balance the quarter-hour maximum energy consumption. Statistical methods are based on historical experience. Persistent models are based on recent measurements. The sky imaging is based on observing recent cloudiness situations; therefore, its prediction for the near future is the most promising one.

7.1.2 MODELLING PV AND BATTERY STORAGE

Learning from irradiance measurements and ground truth sky images improves the performance of predictive energy management systems incorporating photovoltaic power sources (PV) by providing precise power production estimation.

The measured data from the on-site feedback sensor are uploaded into a specific time-series database, which allows the system to react to unpredictable weather events.
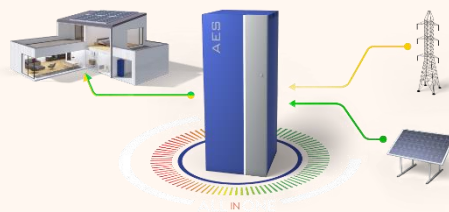
Fig. 21 Example of Home Energy Storage (HES) benefiting from PV Forecast.

The main benefits of PV Forecast services are increased efficiency of any PV / Battery system and reduction of weather-related risks:

- Energy storage scheduling (AI) in response to PV production forecast,

- EV charging infrastructure scheduling,

- Reliable and efficient prediction for spot market trading,

- Efficient management of aggregating solar and storage (VPP),

- Useful for wholesale price users such as generators, network operators, retailers,

- Accurate PV production forecasting to stabilize and secure grid operation (Frequency response),

- Electricity demand, Peak shaving.

A holistic approach to energy optimization and management problematics in the context of external signals can deliver not only the compliance of smart energy systems with the grid but also transform them into flexibility providers that solve the conformity of the non-smart systems incorporating intermittent power sources.

7.2 UTRECHT DEMO

In the Utrecht demo, the PV forecasting method uses cloud detection cameras, meteorological station data, and sensors measuring irradiation and temperature across 1100 Building-Integrated and Building-Applied Photovoltaic panels. This integrated approach enhances the accuracy of PV energy production forecasts by using real-time weather data. The system continuously gathers and processes this data to predict solar energy production in real time and manages energy flows within the building's system to balance generation with consumption needs. The forecasts improve energy use and storage efficiency, informing decisions about when to store or draw energy from batteries. This maximizes the self-consumption of solar power, reduces reliance on the grid, and optimizes energy costs through dynamic battery management.

- The PV Forecasting Method: Uses cloud detection cameras, meteorological data, and weather variables integrated into an AI to provide short-term solar forecasting.

- How Forecasting Works: Continuously gathers and processes data to predict real-time solar energy production and manage energy flows (15-second resolutions).

- Integration in Battery Storage Management: Informs decisions on storing excess energy during high production and drawing energy during low production, optimizing self-consumption, and achieving peak shaving to reduce grid reliance.

7.2.1 PV FORECASTING MODEL AND BATTERY STORAGE

The Fig. 22 provides an overview of a solar forecasting project for Building-Integrated Photovoltaic (BIPV) and Building-Applied Photovoltaic (BAPV) systems in Utrecht. It will take place in the Overvecht and Kanaleneiland-Zuid districts, as highlighted on the accompanying map.

Fig. 22 Methodology and Implementation of PV Forecasting for Building-Integrated and Building-Applied Photovoltaic (BIPV/BAPV) Systems in Demo Utrecht.

Two cloud cameras will be installed to predict PV production using short-term solar forecasting accurately, and the methodology involves several key steps:

- Sky Image Acquisition: Raw images of the sky are captured (every 15 seconds) using sky imagers installed at strategic locations.

- Preprocessing: These images undergo preprocessing steps, including un-distortion, cropping, and masking to isolate relevant areas of the sky.

- Cloud Forecasting: Processed images are used for cloud recognition and cloud motion modeling. Image segmentation helps identify cloud cover percentages and classify sky conditions (e.g., clear, partly cloudy, overcast). An example of the pre-processed image where clouds are detected is shown in Fig. 23.
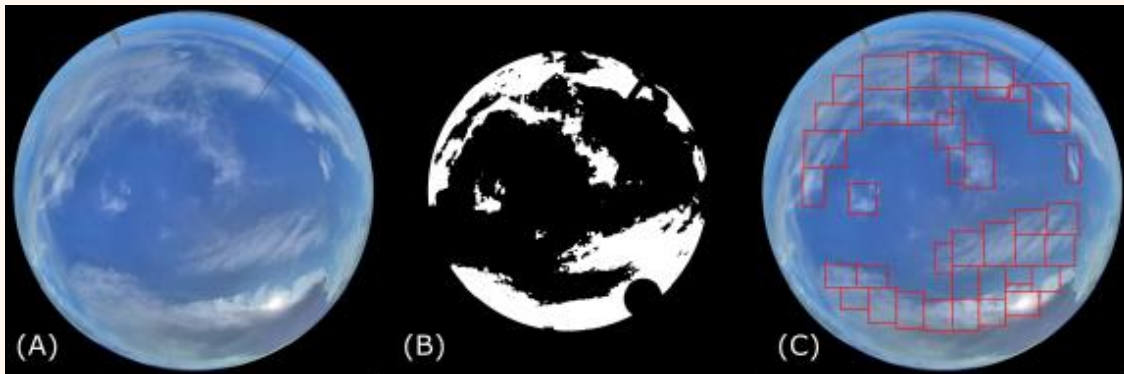
Fig. 23 Figure (A) shows a photo that is analyzed by the SVM, figure (B) shows the cloud mask as identified by the SVM, and figure (C) shows the corresponding cloud blocks that were determined.

- Direct Forecasting: This step uses preprocessed images and weather data to predict solar irradiance directly. Techniques such as Machine Learning Models (Support vector Machine Learning (SVM)) are employed to extract features from the images for accurate forecasting.

- Final Predictive Results: The forecasting system integrates various inputs, including historical PV power outputs, forecasted Irradiance measurements, and weather variables, to produce final predictions of PV power outputs. The diagram below (Fig. 24) illustrates the detailed workflow:
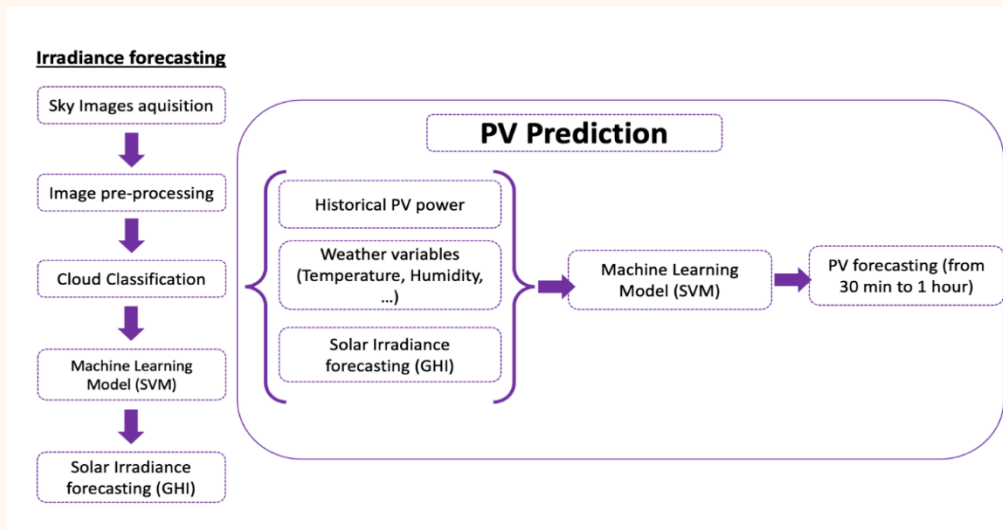

Fig. 24 Flowchart of the methodology implemented in PV forecasting.

Battery storage systems are critical for managing the variability of solar power. In our project, two 35 kWh batteries are installed to enhance energy efficiency through:

- Peak Shaving: The system proactively manages energy demand to eliminate short-term demand spikes. This reduces the peak load on the grid, optimizing energy costs.

- Self-Consumption: By storing excess solar energy during periods of high production, the system ensures this energy is available during low production periods, maximizing self-consumption and reducing reliance on the grid.

We use several key equations to model the battery storage and optimize its performance, as explained in D7.6. The objective function combines two terms, one for minimizing peak demand and the other for

maximizing PV self-consumption. The peak demand term can be defined as the maximum power demand during a given period (e.g., a day or a month). The optimization function considers both energy consumption and peak demand. The objective is to minimize peak demand, which is the focus of the function being optimized.

$$\min_{L(t)_{max}<x<L(t)_{min}} f(x) \tag{32}$$

$$f(x) = \left| C_{batt} - \left(\max \int_{t_0}^{t} (L_i(t) - x)\mathrm{d}t - \min \int_{t_0}^{t} (L_i(t) - x)\mathrm{d}t \right) \right| \tag{33}$$

where C_{batt} is the battery energy capacity, L_i is the load ($i = a, b$ – power measured at the point a or b, for the whole building aggregated or only the facilities side, respectively), x is the shave level, as seen in the schematic in Fig. 25, representing the case study of the connections to the grid with different systems within the building. The PV self-consumption term can be defined as the percentage of PV energy consumed on-site instead of being exported to the grid. The PV self-consumption term, defined as the percentage of PV energy consumed onsite rather than exported to the grid, is maximized using the objective function max $g(x)$, more details can be found in D7.6.

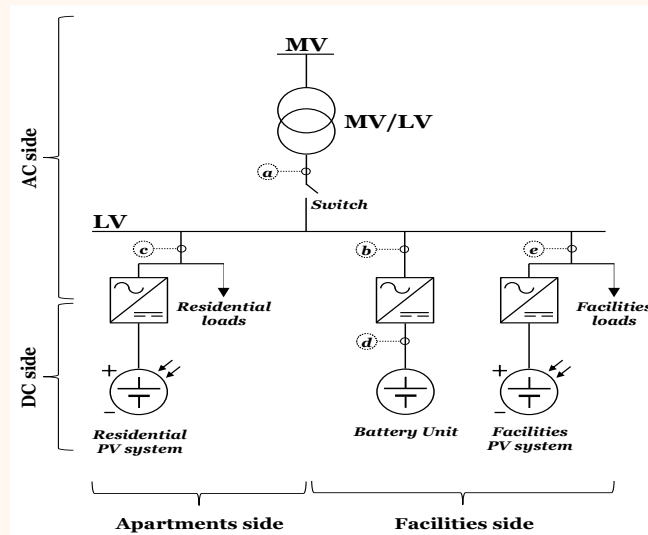

Fig. 25 Schematic of the case study illustrating the connections to the grid with different systems within the building.

Results

Our PV forecasting model, developed and validated using data from sky imagers, demonstrates significant accuracy in predicting short-term solar irradiance. Although we anticipate having the sky imager data from the case study building by November, we have already applied our forecasting model to a nearby building in Overvecht. As shown in Fig. 26, the comparison between the forecasted and actual PV power outputs reveals a high degree of accuracy, validating the effectiveness of our model.
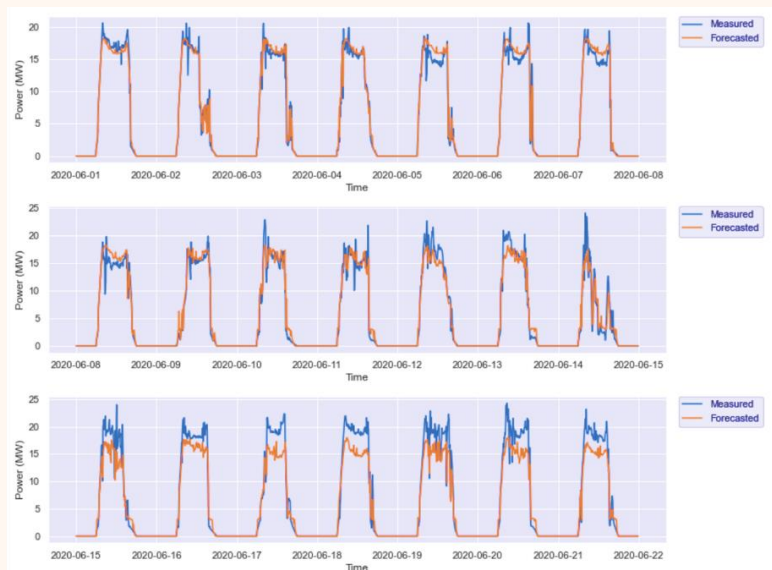
Fig. 26 PV power forecasted vs measured.

The integration of Renewable Energy Sources (RES), energy storage, and Energy Management Systems (EMS) aims to increase self-consumption and minimize peak demand via Battery Energy Storage Systems (BESS) using real-time energy consumption and production data. We can study scenarios over large timeframes by employing All-Sky-Imagers for solar forecasting, as depicted in Fig. 27. The left side of this figure presents the PV production and corresponding consumption patterns during the winter season, showing a mismatch between production and consumption. This highlights the need for efficient energy storage and management to minimize grid dependency and optimize energy usage, as shown in Fig. 27 on the right. The control algorithm, combining PV production forecasting and battery decision-making, provides insights for further development and integration into the building's energy management system.
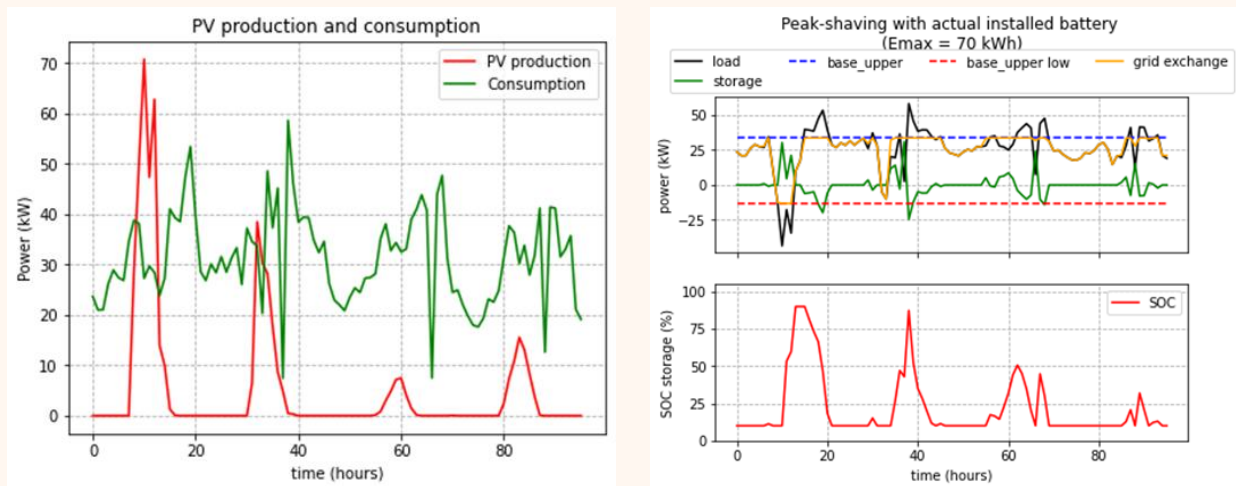

Fig. 27 On the left, PV production and consumption. On the right, peak-shaving with a 70 kWh battery. The data for the whole building are shown in the winter.

Our comparison of the case study, presented in Fig. 27, indicates that the virtual distribution of electricity can be effectively modeled and compared to other buildings, offering insights into the benefits of virtual distribution for self-consumption and overall energy performance.

By implementing these methods and using these formulas, our system ensures optimal PV forecasting and battery storage management performance, contributing to efficient energy use and sustainability goals. More detailed information on the methods can be found in D7.5 and D7.6.

8   LOW-ORDER MODELS FOR THE LOWEX SYSTEM CONTROL (OSLO DEMO)

The Norwegian demo case is the Voldsløkka School and Cultural Area, located in Oslo. The school complex consists of multiple buildings with a total gross building area of approximately 14,000 m² (for more detail, see D6.1). The school features a variety of HVAC technologies implemented in different parts of the buildings, such as ground source heat pump (GSHP), district heating (DH), and PV panels on the building facades and roof. This study will focus on modeling and controlling the low-temperature heating and high-temperature cooling HVAC system (LowEx energy system), which is centered around a GSHP to provide indoor climate control for the S-building of the school complex.

8.1 LOWEX ENERGY SYSTEM

The LowEx HVAC system is specifically designed to enhance the efficiency of ground source heat pumps (GSHPs). While the individual components of this system are not new, their innovative integration is what sets it apart. The performance of heat pumps, measured by the coefficient of performance (COP), largely depends on the temperature differential between the heat source and the cooling source. The COP indicates the ratio of useful heat output to the input energy used by the compressor. To maximize COP, the temperature difference between the sources is minimized, allowing the system to operate with supply temperatures close to the desired indoor temperature.

This system employs a combined radiant heating and cooling approach, maintaining temperature differences between the room design temperature and the fluid as low as 5 K. This configuration allows the same infrastructure to provide both low-temperature heating and high-temperature cooling in conjunction with the GSHP. As a result, the heat pump operates at high efficiency, leading to projected energy consumption between 3 to 10 kWh/m² per year and significantly lowering compressor power peaks. Additionally, the LowEx system is cost-effective and environmentally friendly, as it leverages existing infrastructure, thereby reducing both costs and embodied energy (for more detail, see D9.1).

The thermal needs of the S-building are served by a GSHP, which covers approximately 80-90 % of the energy demand for space heating. District heating is planned to be used as a secondary heat source for peak loads on the coldest days. Space cooling is primarily based on a free cooling concept, where the brine circuit from the energy wells can bypass the heat pump and be directed to the heat exchangers for the secondary HVAC circuits in the building. The GSHP evaporator can also deliver cooling if desired, e.g., with electricity supplied from the PV panels.

The LowEx system distributes heating or cooling to the building spaces via Thermally Activated Building Systems (TABS) and ventilation heating and cooling. TABS is a method of distributing thermal heat to the building's spaces by utilizing large thermal mass to efficiently leverage the thermal storage capacity of the building structure. In the Oslo demo, TABS is installed with hydronic circuits integrated into floor separators (concrete slabs). TABS largely relies on radiant heat transfer to regulate the air temperature in the building spaces. The same equipment and infrastructure can be used for both heating and cooling

in the building. Heated or cooled water can be delivered to the TABS, and a combined heating and cooling coil can be used for the ventilation system. Adjustable shunting valves can pass through water coming either from the GSHP or from bypass-circuits.
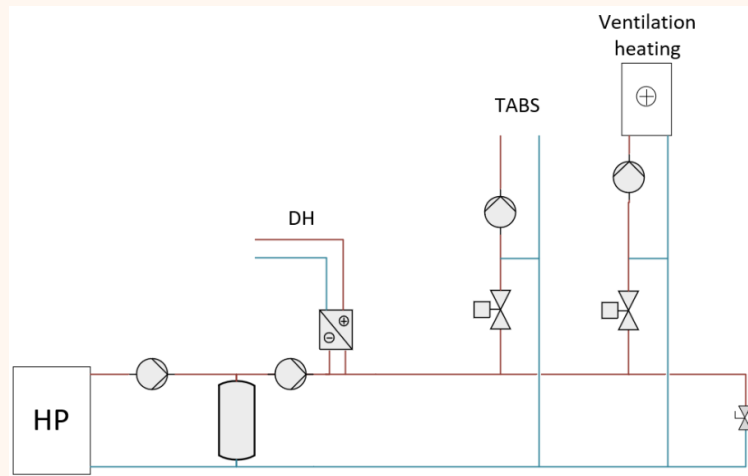

Fig. 28: Simplified sketch of the LowEx-system in the Oslo demo, with the HVAC components and circuits that will be modeled in this study.

8.2 MODELS FOR THE LOW-EX SYSTEM

8.2.1 FLEXOR MODEL

A SINTEF-developed optimization framework called FLEXor will be used to integrate low-order models for various components within the LowEx system. FLEXor is tailored to optimize the use of flexible resources in a building while considering external factors like weather conditions and energy prices, all within certain constraints. The tool addresses three types of flexibility: fuel-switch flexibility, storage flexibility, and comfort flexibility. Comfort flexibility involves permitting a range of acceptable indoor temperatures, enabling energy storage within the building's thermal mass.

Fig. 29 shows an overview of the FLEXor model. The description of the FLEXor model in this section is based on and further described in [25].

The heat source components are modeled in steady-state to avoid non-linearities, where efficiencies of components (e.g., heat pump COP) are based on known properties like weather forecasts instead of variables within the optimization problem, such as produced heat.
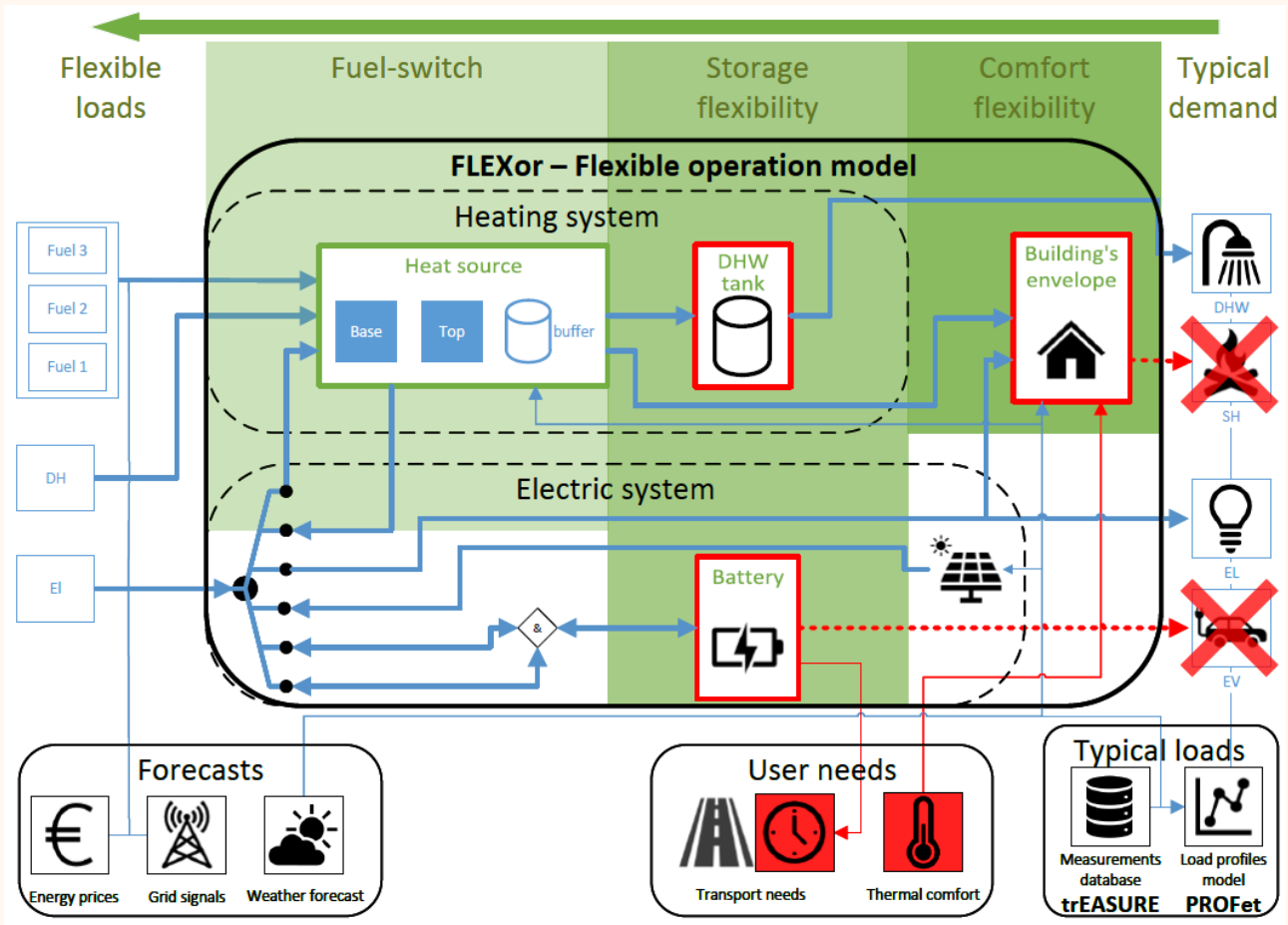
Fig. 29: FLEXor optimization model (SINTEF).

Thermal storage components use reduced-order, linear time-invariant (LTI) state space models. Building energy modeling often employs the RC analogy, where thermal resistances and capacitances correspond to electrical resistances and capacities. The general state space formulation is provided in Equation (34)–(35).

$$dX(t) = A(\Theta)X(t) + B(\Theta)U(t) + E(\Theta)D(t) \tag{34}$$

$$Y(t) = CX(t) \tag{35}$$

where $X(t)$ is the state vector, usually representing internal temperatures in building energy modeling. $U(t)$ is the vector of controllable inputs, representing, e.g., heat from local heating units or mechanical ventilation. $D(t)$ are disturbances like, e.g., solar radiation or internal heat gains. Matrices A and B are parameterized by Θ, while matrix C connects the model's states (predicted temperatures) to the measured outputs $Y(t)$ (measured temperatures). A significant advantage of the LTI state space model is its ability to be directly transformed into a linear programming (LP) optimization problem [26].

In its LP form, the LTI model is represented by a set of constraints (Equation (36)). The heating system in the local building spaces can only emit a limited amount of heat. This is accounted for with a maximum heat emission ($\overline{u}$). Additionally, an indoor temperature constraint creates a thermal comfort band with upper ($\overline{y}$) and lower ($\underline{y}$) limits. To account for situations where maintaining the temperature within this

range is infeasible (such as during periods with warm weather), the temperature constraint is treated as a soft constraint. Any deviation from the temperature constraint (δ) is penalized in the objective function with a penalty factor (ρ). This formulation results in the following optimization problem for a minimum cost objective:

$$x_{k+1} = Ax_k + Bu_k + Ed_k,$$

$$y_k = Cx_k$$

$$\underline{y}_k - \delta_k \leq y_k \leq \overline{y}_k + \delta_k \qquad (36)$$

$$\underline{u}_k \leq u_k \leq \overline{u}_k$$

$$\delta_k \geq 0$$

In the complete FLEXor model, constraints are assessed separately for each sub-model, whereas the objective function is based on the total energy vector imports (see left side of Fig. 29). Additionally, balance constraints ensure proper connections between the components.

8.2.2 HEAT PUMP MODEL IN FLEXOR

The core of the heat pump model is a straightforward calculation, as illustrated in Equation (37), where y_{in} represents the electricity input to the heat pump, q_{SH} is the heat output for space heating, and COP_{SH} is the coefficient of performance of the heat pump. The heat pump operation is constrained by conditions in Equation (38), where $Q_{HP,SH}$ denotes the heat pump's capacity for space heating. The two sub-models – constant performance model and temperature-dependent – primarily differ in the calculation of COP_{SH} [27].

$$y_{in}(t) = \frac{q_{SH}(t)}{COP_{SH}(t)} \qquad (37)$$

$$q_{SH}(t) \leq Q_{HP,SH}(t) \qquad (38)$$

Performance models

The heat pump performance can either be modeled as a temperature-dependent model (Fig. 30), or a constant performance model in FLEXor. The temperature-dependent model requires the three input parameters given in the constant performance model: installed capacity and two nominal COPs. There are three additional input parameters: temperature of the heat source, supply temperature for space heating, and supply temperature for DHW preparation. For archetype case studies, the model uses performance tables for heat pumps from the Norwegian Standard SN-NSPEK 3031:2021 for the calculation of the heat pump performance. Tab. 5 shows example calculations of a GSHP in typical Norwegian conditions. For each timestep during the optimization, the heat delivery (Q_{HP}) capacity and the COP for space heating are calculated by multiplying the installed capacity of the heat pump by the factors interpolated based on the table. The parameters can be tuned for case-specific studies to fit the installed heat pump.

However, the source and supply temperature in GSHP systems can be quite stable, where the temperature-dependent performance can be simplified to a constant performance model without significant loss of accuracy.
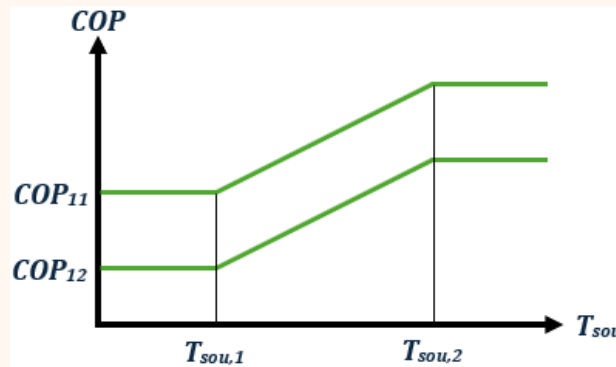

Fig. 30 Temperature-dependent performance model for COP of heat pump, based on SN-NSPEK 3031:2021.

Tab. 5 Table for calculating heat delivery capacity and COP for GSHP, ASHP, and A2A heat pumps, based on SN-NSPEK 3031:2021.

		Q_{HP}			COP		
		T_{sou}			T_{sou}		
	T_{sup}	-5	0	5	-5	0	5
GSHP	35	0.92	1	1.15	0.78	1	1.1
	55	0.82	0.91	1	0.43	0.58	0.73

8.2.3 BUILDING ENVELOPE MODEL IN FLEXOR

The envelope model is an RC model with 3 resistances and 3 capacitances (3R3C) and is shown in Fig. 31. The model is a set of linear differential equations describing the heat flows in the heated spaces of a building [28]. To use FLEXor to control the indoor climate, parameters representing constant coefficients in the equation set must be determined, e.g., heat capacities and thermal resistances. The coefficients can be set for archetype models based on representative values for the archetype category. For a specific building, the parameters can be estimated with building measurement data and model identification methods like e.g. CTSM [29].
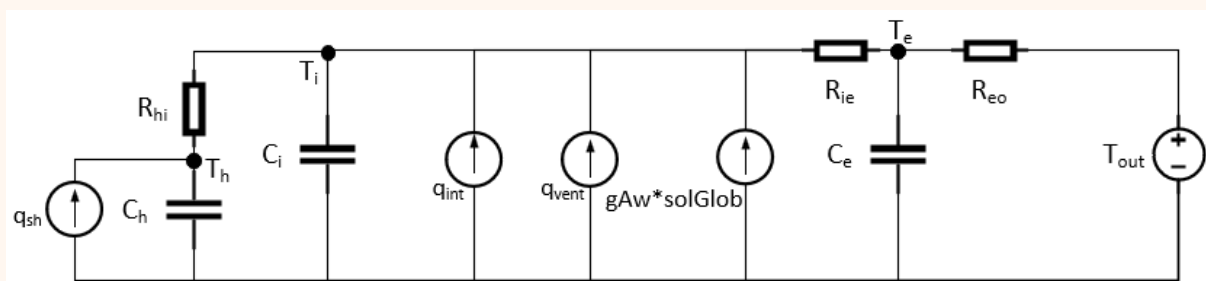

Fig. 31 RC diagram of building envelope model in Flexor.

The model includes 3 state variables that represent temperatures at different parts of the building and are defined by the Equations (39)(41), where the parameters of the equations are explained in Tab. 6.

$$dT_i = \frac{1}{C_i R_{hi}}(T_h - T_i)dt + \frac{1}{C_i R_{ie}}(T_e - T_i)dt + \frac{solGlob \cdot gA_w}{C_i}dt + \frac{1}{C_i}q_{vent}dt + \frac{1}{C_i}q_{int}dt \quad (39)$$

$$dT_h = \frac{1}{C_h R_{hi}}(T_i - T_h)dt + \frac{1}{C_h}q_{sh}dt \quad (40)$$

$$dT_e = \frac{1}{C_e R_{ie}}(T_i - T_e)dt + \frac{1}{C_e R_{eo}}(T_{out} - T_e)dt \quad (41)$$

Tab. 6 Parameters in the building envelope model.

Parameters	Description
T_i	Temperature of indoor air
T_e	Exterior surface temperature of building facade
T_{sh}	Surface temperature of local heating unit
T_{out}	Temperature of outdoor air
C_e	Heat capacity of the building envelope
C_i	Heat capacity of the interior building construction
C_h	Heat capacity of the local heating unit
R_{eo}	Thermal resistance between outdoor air and external surface
R_{ie}	Thermal resistance between external and internal surfaces
R_{hi}	Thermal resistance between local heating unit and indoor air
q_{sh}	Heat flux from local heating unit
q_{int}	Heat flux from internal gains
q_{vent}	Heat flux from ventilation

9 REFERENCES

[1] IEA, "Global Status Report for Buildings and Construction 2019 – Analysis - IEA," *IEA 2023*, 2023.

[2] X. Li and J. Wen, "Review of building energy modeling for control and operation," *Renew. Sustain. Energy Rev.*, vol. 37, pp. 517–537, 2014.

[3] L. G. Swan and V. I. Ugursal, "Modeling of end-use energy consumption in the residential sector: A review of modeling techniques," *Renewable and Sustainable Energy Reviews*, vol. 13, no. 8. 2009.

[4] J. A. Fonseca, T. A. Nguyen, A. Schlueter, and F. Marechal, "City Energy Analyst (CEA): Integrated framework for analysis and optimization of building energy systems in neighborhoods and city districts," *Energy Build.*, vol. 113, 2016.

[5] J. A. Candanedo *et al.*, "Control-oriented archetypes: a pathway for the systematic application of advanced controls in buildings," *J. Build. Perform. Simul.*, vol. 15, no. 4, 2022.

[6] D. Yan *et al.*, "Occupant behavior modeling for building performance simulation: Current state and future challenges," *Energy Build.*, vol. 107, pp. 264–278, 2015.

[7] T. Hong, S. C. Taylor-Lange, S. D'Oca, D. Yan, and S. P. Corgnati, "Advances in research and applications of energy-related occupant behavior in buildings," *Energy and Buildings*, vol. 116. 2016.

[8] C. Ding and N. Zhou, "Using residential and office building archetypes for energy efficiency building solutions in an urban scale: A China case study," *Energies*, vol. 13, no. 12, 2020.

[9] R. Mohammadiziazi, S. Copeland, and M. M. Bilec, "Urban building energy model: Database development, validation, and application for commercial building stock," *Energy Build.*, vol. 248, 2021.

[10] C. F. Reinhart and C. Cerezo Davila, "Urban building energy modeling – A review of a nascent field," *Build. Environ.*, vol. 97, pp. 196–202, 2016.

[11] J. Palmer Real, J. K. Møller, R. Li, and H. Madsen, "A data-driven framework for characterising building archetypes: A mixed effects modelling approach," *Energy*, vol. 254, p. 124278, 2022.

[12] M. H. Kristensen, R. E. Hedegaard, and S. Petersen, "Hierarchical calibration of archetypes for urban building energy modeling," *Energy Build.*, vol. 175, pp. 219–234, 2018.

[13] H. G. Bergsteinsson, J. K. Møller, P. Nystrup, Ó. P. Pálsson, D. Guericke, and H. Madsen, "Heat load forecasting using adaptive temporal hierarchies," *Appl. Energy*, vol. 292, 2021.

[14] H. A. Nielsen and H. Madsen, "Modelling the heat consumption in district heating systems using a grey-box approach," *Energy Build.*, vol. 38, no. 1, 2006.

[15] H. Madsen, K. Sejling, H. T. Søgaard, and O. P. Palsson, "On flow and supply temperature control in district heating systems," *Heat Recover. Syst. CHP*, vol. 14, no. 6, 1994.

[16] T. S. Nielsen, "Online prediction and control in nonlinear stochastic systems," *Math. Model.*, no. 84, 2002.

[17] M. Barla, A. Di Donna, and A. Insana, "A novel real-scale experimental prototype of energy tunnel," *Tunn. Undergr. Sp. Technol.*, vol. 87, 2019.

[18] A. Insana and others, "Thermal and structural performance energy tunnels," *Politec. di Torino*, 2020.

[19] A. Insana and M. Barla, "Experimental and numerical investigations on the energy performance of a thermo-active tunnel," *Renew. Energy*, vol. 152, 2020.

[20] M. Barla, A. Di Donna, and A. Perino, "Application of energy tunnels to an urban environment," *Geothermics*, vol. 61, 2016.

[21] M. Baralis, M. Barla, W. Bogusz, A. Di Donna, G. Ryzyński, and M. Zeruń, "Geothermal potential of the ne extension warsaw (poland) metro tunnels," *Environ. Geotech.*, vol. 7, no. 4, 2020.

[22] M. Barla and A. Insana, "Energy tunnels as an opportunity for sustainable development of urban areas," *Tunn. Undergr. Sp. Technol.*, vol. 132, 2023.

[23] T. Huld *et al.*, "A power-rating model for crystalline silicon PV modules," *Sol. Energy Mater. Sol. Cells*, vol. 95, no. 12, 2011.

[24] C. de Boor, "A Practical Guide to Splines," *J. Appl. Math. Mech.*, vol. 60, no. 1, 1980.

[25] G. Barchi, E. D. Maria, H. T. Walnum, M. Bagle, and K. Thunshelle, "Report on strategy for building flexibility," 2024.

[26] R. Halvgaard, N. K. Poulsen, H. Madsen, and J. B. Jørgensen, "Economic Model Predictive Control for building climate control in a Smart Grid," in *2012 IEEE PES Innovative Smart Grid Technologies, ISGT 2012*, 2012.

[27] B. M. Delgado, H. T. Walnum, and I. Sartori, "Heat Pump, solar PV and Battery Systems Modelling The development of simulation and optimization models for energy-flexible operation in the built environment," *ZEN MEMO*, 2023.

[28] P. Bacher and H. Madsen, "Identifying suitable models for the heat dynamics of buildings," *Energy Build.*, vol. 43, no. 7, pp. 1511–1522, 2011.

[29] N. R. Kristensen, H. Madsen, and S. B. Jørgensen, "Parameter estimation in stochastic grey-box models," *Automatica*, vol. 40, no. 2, pp. 225–237, 2004.

10 ACKNOWLEDGEMENTS AND DISCLAIMER

11 APPENDIX A – GLOSSARY OF TERMS

Table A.1 Abbreviations used in the report.

Abbreviation	Description
CPCC	Climate Positive Circular Communities.
ABEM	Archetype building energy model
HVAC	Heating ventilation and air conditioning
RES	Renewable energy source
EMS	Energy management system
DHW	Domestic Hot Water
COP	Coefficient of performance
rBHEs	radial Borehole heat exchangers
GSHP	Ground source heat pump
BESS	Battery energy storage system

12 PARTNER LOGOS

www.greendeal-arv.eu

CLIMATE POSITIVE CIRCULAR COMMUNITIES

ARV